GYROSCOPES BASED ON ACOUSTIC WAVEGUIDES

A Thesis

by

Hakan Çetin

Submitted to the
Graduate School of Sciences and Engineering
In Partial Fulfillment of the Requirements for
the Degree of

Master Science

in the
Department of Electrical and Electronics Engineering

Özyeğin University
August 2016

GYROSCOPES BASED ON ACOUSTIC WAVEGUIDES

Approved by:

Assoc. Prof. G. Goksenin Yaralıoğlu,
Thesis Advisor,
Department of Electrical and Electronics
Engineering,
Özyeğin University

Assoc. Prof. Ayhan Bozkurt
Department of Electrical and Electronics
Engineering,
Sabancı University

Assist. Prof. Cenk Demiroğlu,
Department of Electrical and Electronics
Engineering,
Özyeğin University

Date Approved: 9 August 2016

To my family

ABSTRACT

We propose novel gyroscope architectures based on acoustic waves propagating in a waveguide. This thesis is composed of two parts. In the first part, the fundamentals of the proposed gyroscope are discussed. The new gyroscope will consist of a closed circular waveguide and a piezoelectric transducer, which excites the suitable acoustic modes of the waveguide. The piezoelectric transducer will generate two acoustic waves, which propagate in the opposite directions in the waveguide. When the waveguide is subjected to a rotational motion, due to the Coriolis forces, the acoustic waves that propagate in the opposite directions will gain different amounts of phases. The relative phase difference of these two waves will increase in proportional to the angular velocity of the waveguide. In other words, by measuring the phase difference between these two waves, one can monitor the rate of rotational motion. During our analysis of waveguides, we observed that the resonances of the waveguide structure shift. This is due to the velocity shift of the counter-propagating waves in response to Coriolis force. Based on this observation, we performed in-depth analysis of vibrating gyroscope structures. This analysis constitutes the second part of the thesis.

A typical vibrating gyroscope has two parts which are called drive and sense systems. Until now, the coupling between these two systems has been ignored and they have been analyzed separately. In the second part of this thesis, we demonstrate the analysis of the gyroscope including the coupling between drive and sense systems for the first time. Vibratory gyroscopes have attracted a lot of interest recently with the development of MEMS gyroscopes. These gyroscopes made their way through portable devices and smart phones. Novel gyroscope architectures have been proposed and analyzed in detail. However in most of these analyses, the coupling between

the sense and drive systems were ignored. We analytically show that the drive and sense systems are coupled together via Coriolis force. As a result, resonances of the mechanical structure shift as the rotation rate increases for linear and torsional gyroscope systems. Starting from a simple gyroscope system, we calculated the sense and drive resonant frequency shifts in various configurations. Then, for more complex systems where analytical solution is difficult to obtain, we used commercially available FEM tools to determine the corresponding frequency shift. In general, we found that the shift is small and can be ignored for mode-matched linear vibratory gyroscopes, where Q of the sense system is less than 2500. But for higher Q systems, the frequency shift may affect the linearity of these gyroscopes. This sets a fundamental limit for the linearity of vibratory gyroscopes. Based on our calculations, the non-linearity is above 1% for linear 2-DOF mode-matched vibratory gyroscopes, where Q is above 3000 and for torsional 2-DOF mode-matched vibratory gyroscopes where Q is above 600. Multi-DOF and ring vibratory gyroscopes were also examined. We found that the effect is less pronounced for Multi-DOF gyroscopes.

ÖZETÇE

Akustik dalgaların dalga kılavuzunda ilerlediği yeni dönüölçer yapıları önerilecektir. Bu tez iki bölümden oluşmaktadır. İlk bölümünde, önerilen dönüölçerin temel prensipleri tartışılacaktır. Bu yeni dönüölçer halka şeklinde üretilmiş kapalı bir dalga kılavuzundan ve bunun uygun modlarını tetikleyen bir piezoelektrik çeviriciden oluşacaktır. Piezoelektrik çevirici dalga kılavuzu içerisinde karşıt yönlerde yol alan iki akustik dalga üretecektir. Dalga kılavuzu bir dönme hareketine maruz kaldığında Coriolis kuvvetinin etkisiyle birbirine zıt yönlerde hareket eden akustik dalgalar farklı miktarlarda faz kazanacaklardır. İki dalganın birbirine göre faz farkı dalga kılavuzunun açısal dönme hızıyla doğru orantılı olarak artacaktır. Bir başka deyişle iki dalga arasındaki faz ölçülerek, dönme hareketinin hızını takip etmek olasıdır. Dalga kılavuzunun analizleri sırasında, dalga kılavuzunun rezonanslarının kaydığı gözlemlenmiştir. Bunun nedeni Coriolis kuvvetinin müdahalesiyle karşıt yönlerde ilerleyen dalganın hız kaymasıdır. Bu gözlemlere göre, titreşimli dönüölçerlerin daha derin analizi yapılmıştır. Bu analiz tezin ikinci kısmını oluşturmaktadır.

Tipik titreşimli dönüölçer, sürme ve algılama sistemleri olarak iki parçadan oluşur. Bu zamana kadar, bu iki sistemin karşılıklı etkileşimi (coupling) göz ardı edilmiş ve ayrı ayrı analiz edilmişlerdir. Tezin ikinci kısmında, sürme ve algılama sistemleri arasındaki karşılıklı etkileşimin olduğu analizi ilk defa göstereceğiz. Titreşimli dönüölçerler MEMS dönüölçerlerin gelişmesiyle son zamanlarda çok dikkat çekmiştir. Bu dönüölçerler taşınabilir aletler ve akıllı telefonlar kanalıyla ilerlemiştir. Yeni dönüölçer yapıları detaylı olarak önerilmiş ve analiz edilmiştir. Bu birçok analize rağmen sürme ve algılama sistemleri arasındaki karşılıklı etkileşim göz ardı edilmiştir. Biz ise analitik olarak sürme ve algılama sistemleri arasındaki karşılıklı etkileşimin

Coriolis kuvveti nedeniyle olduğunu göstereceğiz. Bunun sonucunda, lineer ve burulumsal (torsional) dönüölçer sistemlerinin mekanik yapı rezonansları dönme oranı arttıkça kaymıştır. Basit dönüölçer sistemlerinden başlayarak, algılama ve sürme rezonans frekans kaymaları çeşitli konfigürasyonlarda hesaplanmıştır. Daha sonra analitik çözümün elde edilmesinin zor olduğu daha karmaşık sistemler için ticari olarak mevcut olan Sonlu Eleman Metodu, alakalı frekans kaymasının belirlenmesi için kullanılmıştır. Genel olarak kayma, sistemin Q'su 2500'den az olan eşlenik modlu lineer titreşimli dönüölçerler için küçüktür. Fakat, daha yüksek Q sistemleri için, frekans kayması bu dönüölçerlerin lineerliğini etkileyebilir. Bu titreşimli dönüölçerlerin lineerliğine temel bir limit koyar. Hesaplamalarımıza göre, Q'su 3000'den fazla olan 2-serbestlik dereceli eşlenik modlu lineer titreşimli dönüölçerler ve Q'su 600'den fazla olan 2-serbestlik dereceli eşlenik modlu brumsal titreşimli dönüölçerler için lineersizlik 1% dir. Çoklu serbestlik dereceli ve halka titreşimli dönüölçerler de incelenmiştir. Bu etkinin çoklu serbestlik dereceli dönüölçerler için oldukça azdır.

ACKNOWLEDGEMENTS

TABLE OF CONTENTS

LIST OF TABLES

LIST OF FIGURES

CHAPTER I

INTRODUCTION

During the World War II, inertial sensors were used for military purposes to control the trajectory of the missiles. Later, inertial sensor-based civilian and military navigation systems were developed for aircrafts and ships. An inertial sensor, which is used for navigation systems, consists of an accelerometer and a gyroscope. In general, the construction of the gyroscope is more difficult and complex than the construction of the accelerometer. Nowadays, fiber optic-based gyroscopes (FOG - Fiber Optic Gyroscope) are widely used for navigation applications. In these devices, a closed loop optical path is formed by wrapping a long piece of fiber, which is a few kilometers in length around a coil. In this optical path, the light obtained from a laser diode propagates in both directions. When the coil is subjected to a rotational motion, phases of the light beams change relative to each other due to the Sagnac effect. By detecting this phase shift in an interferometric configuration, the rotation rate is measured. The fiber optic gyroscopes have a very high stability (Angular random walk: 0.01 deg/$\sqrt{h}$, Bias stability: 0.001 deg/h), and they are used successfully in navigation applications. But since these devices require a long amount of fiber optic cable, their sizes (~ 10 cm^3) and the weights (~ 0.5 kg) are quite high. The main reason for this is the high speed of the light and long wavelength. The light is required to travel a few kilometers to obtain a measurable phase shift and even if the fiber cable is wrapped in a coil, it still occupies a large volume.

On the other hand, with the development of MEMS technology smaller size gyroscopes have been produced for the applications of non-navigational systems since

1980. The first applications of MEMS gyroscopes that measure Coriolis force appeared as camera image stabilization. As the technology allowed producing MEMS gyroscope more cost effectively, these devices were able to get into almost every smart phone and tablet computer. The most basic applications are in games, user interfaces and privacy (air sign − the hand gesture of the user is used for authentication). However, the stability of the MEMS gyroscope (Angular random walk: 0.1 deg/$\sqrt{h}$, Bias stability: 10 deg/h) is much worse than the stability of optical gyroscopes. So this limits the use of MEMS gyroscopes for navigation based applications. There is a need for gyroscopes which are inexpensive but have high stability.

The aim of this thesis is to discover the design method of a gyroscope that will not only have the potential to reach the stability of the fiber optic gyroscopes but also compete with MEMS-based gyroscope in respect to size and power consumption. The main reason of using acoustic wave is that these waves have much slower speed compared to the speed of light. A gyroscope can be made by using much smaller waveguides than optical fibers, because speed of the acoustic wave is one million times smaller than the speed of light. Besides piezoelectric transducers consume much less power than laser diodes do. Therefore, one can built more power efficient gyroscopes using acoustic waves.

1.1 Thesis Contribution

The main contribution of this thesis is the introduction of a novel gyroscope structure where acoustic waves in a waveguide are used to detect Coriolis force. When the acoustic waves travelling in the opposite directions are exposed to a rotation, their wave speeds change. By detecting the speed change, one can monitor the rotation rate. The proposed gyroscope consists of a piezoelectric transducer and a circular closed loop waveguide. The cross section of the loop is also circular. To be able to design and optimize such gyroscope systems one needs to analyze the dispersion

curves of the circular waveguides. In the analyses section, we present the calculation of dispersion curve for circular waveguides. We also present verification of the calculations with finite element method. Then, we describe how to choose appropriate modes and other details of the gyroscope. In the second part of the thesis, we present analysis of vibratory gyroscopes. Vibratory gyroscopes have drive and sense systems. In the previous analysis approaches, these two systems were assumed to be uncoupled and they were analyzed separately. We show that the coupling between these two systems can not be ignored for high rotation rates. The coupling is due to the Coriolis force and the effect of centrifugal force is minimal. We also show that the coupling sets a fundamental limit for the linearity of the gyroscope systems.

CHAPTER II

BACKGROUND

2.1   Mechanical Gyroscopes

Mechanical gyroscopes were discovered in the 19th century by Jean-Bernard-Léon Foucault, as shown in Fig. 2.1. In a gyroscope frame, the wheel is mounted in a double-axed gimbal. As the wheel is rotated, the force of gravity is applied on the wheel's center of mass and the wheel does not affected by any torque. So, when the rotation is applied on the gyroscope, the double-axed gimbal starts to tilt. Whereas, the spinning wheel maintains its position regardless to the rotation due to the conservation of angular momentum. This feature of gyroscopes enables to measure the rotation rate of systems.

Figure 2.1: Gyroscope invented by Léon Foucault and built by Dumoulin-Froment in 1852. Photo taken at National Conservatory of Arts and Crafts museum, Paris.

The first workable gyrocompass was developed by H. Anschtz-Kaempfe in 1908. Furthermore, gyroscopes have been used for automatic steering in missiles, stabilized bombsights, and platforms to carry guns in World War II. More recently, these traditional gyroscopes are still used for inertial guidance systems, where they are used by orbital spacecraft and control systems of some satellites, though mechanical systems are being replaced by optical gyroscopes.

2.1.1 Coriolis Effect

All mechanical gyroscopes utilize the Coriolis acceleration in order to detect the rotation rate. The physical interpretation of Coriolis force is well known, in this section we will explain the Coriolis force in conjunction with MEMS gyroscopes. Coriolis force affects the linear type MEMS gyroscope structures in rotating reference frame and the torsional type gyroscope structures in stationary reference frame. Thus, the principle of operation for mechanical gyroscopes can be comprehended better by analyzing the motion of a rotation-induced body based on reference frames.

Two reference frames are shown in Fig. 2.2, as the stationary reference frame (Frame A) and the rotating reference frame (Frame B). An object located at r_A in Frame A can be also represented in Frame B as an object located at r_B. The position of Frame B is located at R in Frame A. Θ represents the orientation of rotating Frame B and Ω is the angular velocity vector of Frame B, $(\Omega = \dot{\Theta})$ [1].

The time derivatives of a vector r_A and r_B are given as:

$$\dot{r_A}(t) = \dot{r_B}(t) + \dot{\Theta} \times r_B(t) \tag{2.1}$$

The acceleration of a body in Frame B is calculated as:
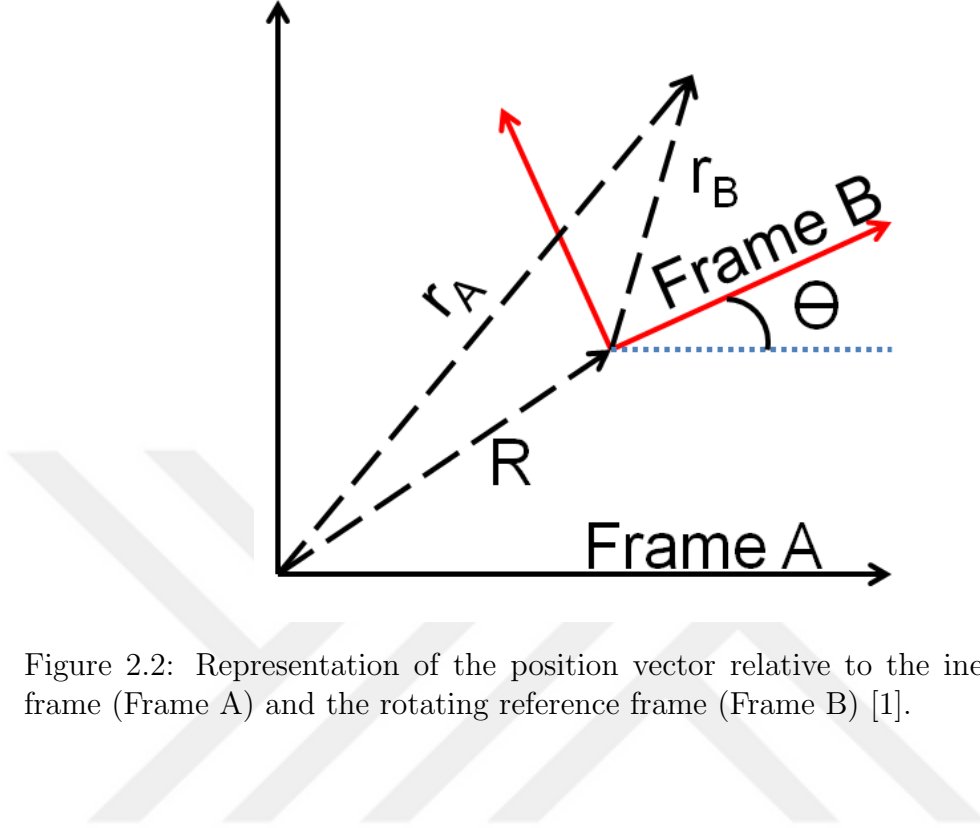
Figure 2.2: Representation of the position vector relative to the inertial reference frame (Frame A) and the rotating reference frame (Frame B) [1].

$$r_A(t) = R(t) + r_B(t) \tag{2.2}$$

$$\dot{r_A}(t) = \dot{R}(t) + \dot{r_B}(t) + \dot{\Theta} \times r_B(t) \tag{2.3}$$

$$\ddot{r_A}(t) = \ddot{R}(t) + \ddot{r_B}(t) + \dot{\Theta} \times \dot{r_B}(t) + \dot{\Theta} \times (\dot{\Theta} \times r_B(t)) + \ddot{\Theta} \times r_B(t) + \dot{\Theta} \times \dot{r_B}(t) \tag{2.4}$$

For simplicity, v_B and a_B can be defined as the velocity and acceleration vectors in Frame B respectively; a_A, as the acceleration vector in Frame A; A, as the linear acceleration in Frame B.

$$a_A = A + a_B + \dot{\Omega} \times r_B + \Omega \times (\Omega \times r_B) + 2\Omega \times v_B \tag{2.5}$$

The translational motion between the two reference frames A can be ignored in order to focus on the rotational motion. So, the 2.5 can be rewritten in terms of a_B:

$$a_B = a_A - \dot{\Omega} \times r_B - \Omega \times (\Omega \times r_B) - 2\Omega \times v_B \tag{2.6}$$

13

This analysis can be applied for the proof-mass of vibratory gyroscopes in order to understand their dynamics. According to Newton's Laws, the force coming from the (2.6) consists of two components: $F_B = F_A + F_{Fict}$. So, the fictitious force is described as:

$$F_{Fict} = F_{Coriolis} + F_{Euler} + F_{Centrifugal} \tag{2.7}$$

where,

$$F_{Coriolis} = -2m(\Omega \times v_B) \tag{2.8}$$

$$F_{Euler} = -m(\dot{\Omega} \times r_B) \tag{2.9}$$

$$F_{Centrifugal} = -m(\Omega \times (\Omega \times r_B)) \tag{2.10}$$

The rotation rate can be considered as a constant value. So, the Euler force goes to zero in (2.7). We will use the Coriolis and centrifugal terms for the analysis of vibratory gyroscopes in Chapter 4.

2.1.2 MEMS Vibratory Rate Gyroscopes

In traditional gyroscopes, rotating parts have been used for a long time, which caused bearing wear and friction problems due to their operation principles. Because of these problems, people avoid using rotating parts in MEMS gyroscopes. So, the most of MEMS gyroscopes in industry start to use vibrating mechanical elements to sense angular rate. Not having any detached moving parts makes the fabrication of gyroscopes easier and suitable for miniaturization by micromachining processes, which leads them to be a competitive alternative. These types of gyroscope are called MEMS Vibratory Rate Gyroscopes (VRGs).

VRG is composed of two mechanical systems; drive and sense. The drive system has a vibratory motion which is coupled to the sense system, as the gyroscope is
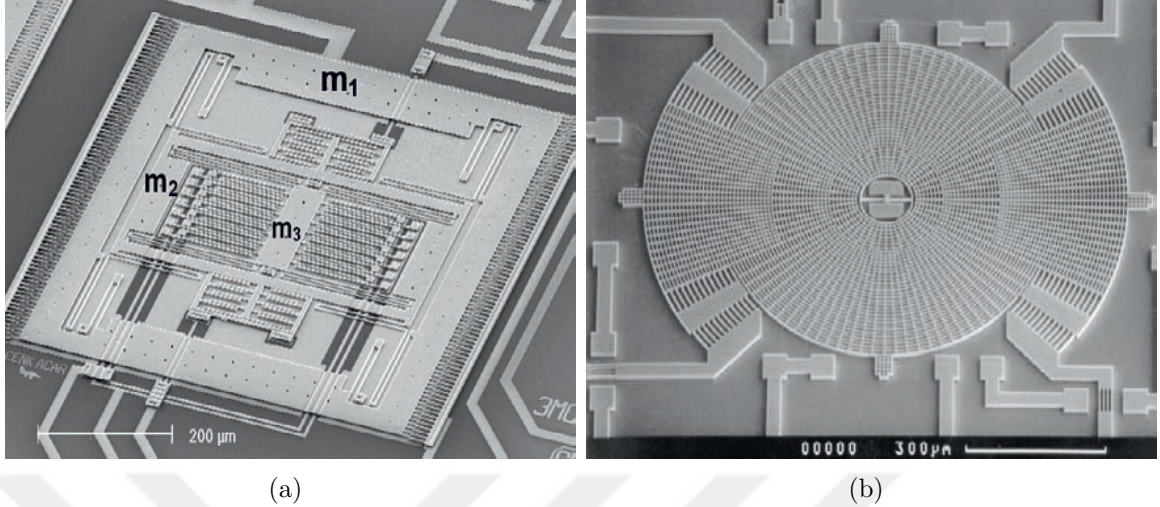
Figure 2.3: (a) Linear vibratory gyroscope [1]. (b) Torsional vibratory gyroscope [2].

subjected to a rotational motion. In most of VRGs, energy transfer is occurred between two modes of the system due to Coriolis acceleration since the drive system excites the first mode. There are two types of VRGs, which are linear ones in Fig. 2.3(a) and torsional ones in Fig. 2.3(b). These VRGs have drive-mode oscillators that generate a constant linear momentum for linear VRGs and angular momentum for torsional VRGs. The drive-mode vibration, which is excited by the drive-mode oscillator, is coupled with the orthogonal Coriolis force or Coriolis torque due to the applied rotation, which is measured by the sense-mode accelerometer. These drive-mode oscillator and sense-mode accelerometer can be chosen as either linear or torsional resonators regarding to types of VRGs. For linear VRGs, the linear drive oscillator is used for exciting the Coriolis force and for torsional VRGs, the rotary drive oscillator is used for exciting the Coriolis torque in order to measure rotation rate.

Maximum gain can be obtained by matching the drive and sense resonances of VRGs. Also, one can design VRGs as non-mode matched gyroscopes by sacrificing the gain and sensitivity. For mode-matched VRGs, two main problems have been revealed as fabrication problems and Coriolis coupling effect. Fabrication problems

cause frequency mismatch between drive and sense modes, which can be compensated by tuning systems. In the second place, the Coriolis coupling effect causes frequency shift for both the drive and sense modes during the applied rotation. The in-depth analysis of the Coriolis coupling effect for vibrating gyroscopes will be provided in Chapter 4.

2.1.3 SAW Based MEMS Gyroscopes

Surface acoustic waves (SAWs) were discovered in 1885 by Lord Rayleigh. They propagate on the surface of an elastic medium. The amplitudes of SAWs decay exponentially regarding to depth into the substrate, due to the concentration of their energy near the substrate surface, as shown in Fig. 2.4(a). Piezoelectric substrates such as lithium niobate, lithium tantalate, and quartz are generally preferred as the elastic medium. Piezoelectric effect of these materials is used for producing SAWs. Working principle of the piezoelectric effect is based on the electromechanical interaction between mechanical stress and electrical charges of the material, which allows converting the mechanical energy to the electrical energy and vice versa. Piezoelectric materials are excited by interdigital transducers (IDTs), which are patterned on their surfaces. IDTs can be used as transmitters, receivers and reflectors. Electric field between transmitter IDTs , which are created by applying electrical input on the electrodes, forms the particle motion in the piezoelectric substrate. As a result, this piezoelectric coupling induces SAWs. On the other hand receiver IDTs, which are charged by the arrived acoustic waves, detect these excited SAWs by means of the reciprocity of the piezoelectricity.

As shown in Fig. 2.4(b,d), SAWs are the combination of longitudinal and shear waves due to their particle motion in both z and y direction with a phase difference of $\pi/2$. One of the most important points for the particle motion of SAWs is the change of compressional motion to dilatational motion regarding to depth into the

substrate. u_y and u_z decay exponentially with depth inside the substrate material. So in the light of these points, it is suggested to use substrates whose thickness is at least five wave length in order to avoid any reflection from the bottom surface by Supriyo Datta, as shown in Fig. 2.4(c).
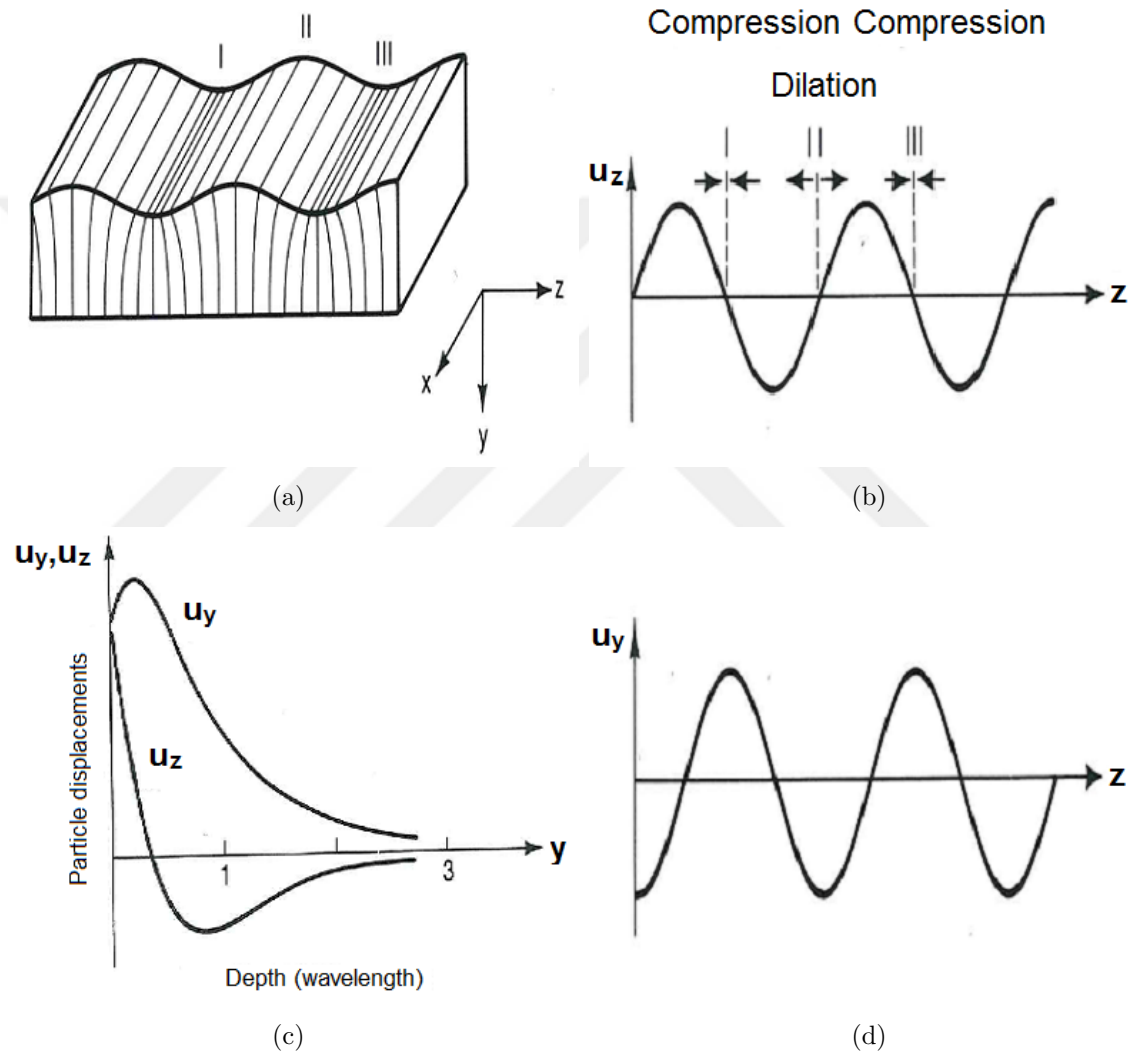
Figure 2.4: (a) Surface wave in a semi-infinite solid; (b) u_z vs. z at the surface; (c) Variation of particle displacement with depth; (d) u_y vs. z at the surface [3].

Gyroscopes, which utilize the SAWs, were studied in the literature [4, 5, 9–15]. They used the simple device, which has a piezoelectric substrate with IDTs as shown in Fig. 2.5, in order to measure the rotation rate.

In Fig. 2.5, SAWs are produced on a piezoelectric substrate with two IDTs.

The transmitter IDT produces the SAWs and the IDT converts received waves into electrical signals. As this device is rotated around the x_2-axis, velocity of the SAW changes. This produces a phase shift on the received electrical signal. One can detect the phase shift in an oscillatory circuit. The oscillation frequency which is determined by the SAW velocity can be measured to monitor the rate of rotation.
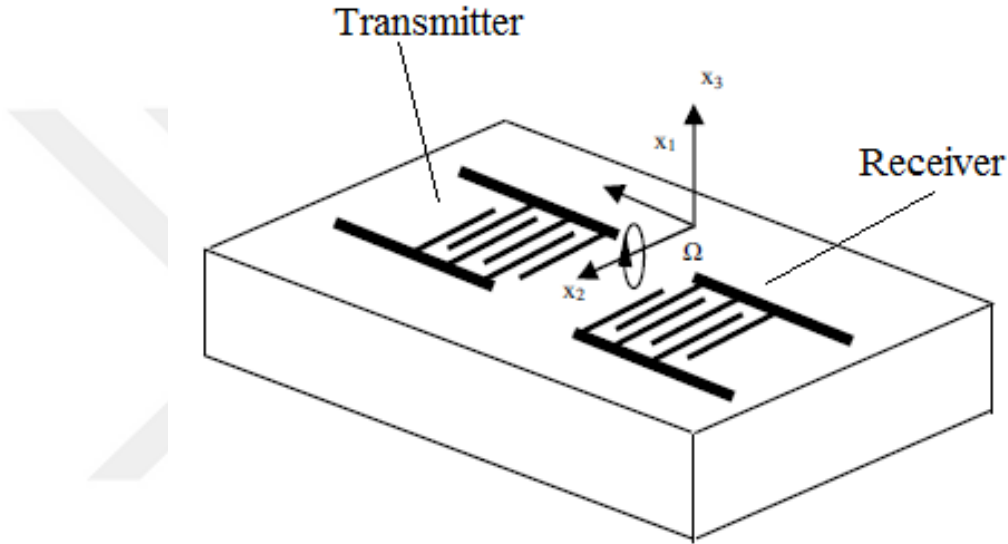
Figure 2.5: Piezoelectric substrate with IDTs [4].

In general, it is not possible to make a gyroscope by utilizing SAWs with high sensitivity. The Coriolis force affects the particles near and away from the surface oppositely, as shown in Fig. 2.4. This is the reason why the effect of Coriolis force on SAWs is minimal. Besides, this Coriolis Effect can be equal to zero for some materials as mentioned in Lao's article [16]. In this article, it was indicated that the effect of Coriolis force on the velocity of SAWs depends on the Poisson's ratio. When the Poisson's ratio is 0.27, this Coriolis Effect is zero. Because of this reason, SAW based devices are not the best choice for using as gyroscopes.

Varadan designed a different SAW based gyroscope in order to solve this problem [5]. The size of this device is 5 mm to 5 mm. Metal squares are placed on the propagation path of SAW, as shown in Fig. 2.6. These metal squares start to move
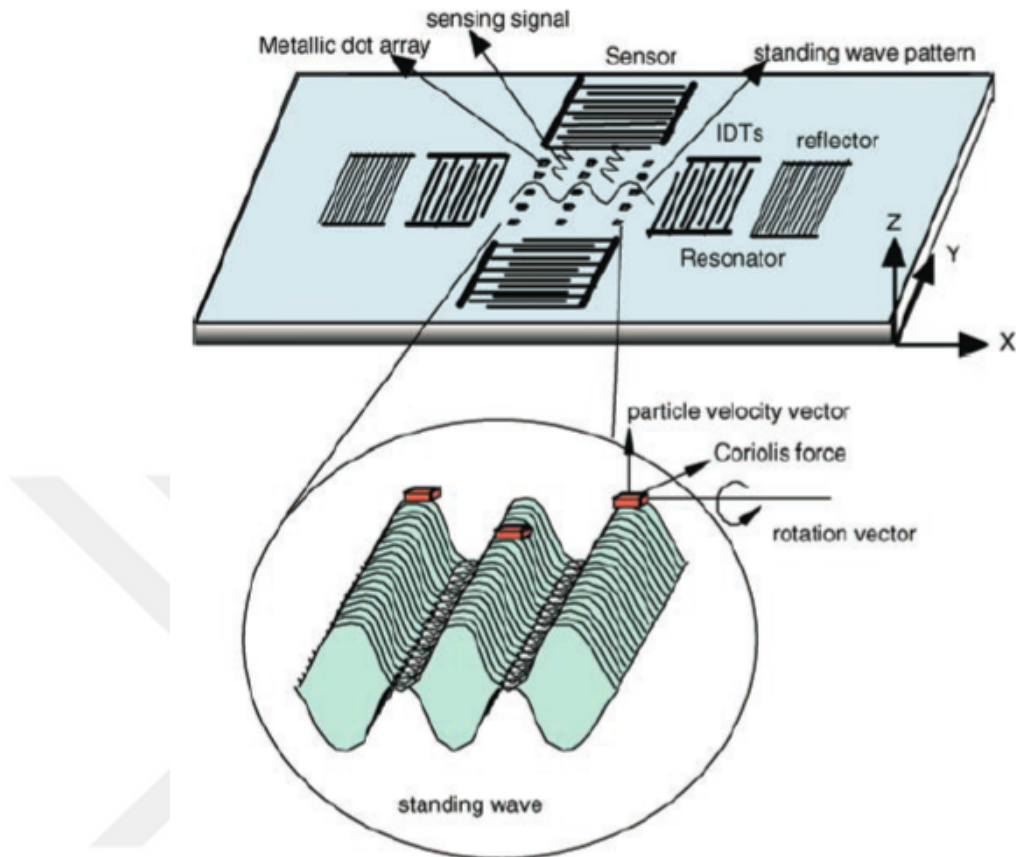
Figure 2.6: SAW based gyroscope [5].

up-down (orthogonal to surface) and back-forward (in the propagation direction) while the SAW is propagating through them. As an angular velocity is applied about the X-axis during this propagation, the Coriolis force is going to be induced about the Y-axis, which is orthogonal to up-down movement of metal squares. This force produces second SAW orthogonal to first SAW. The amplitude of second SAW is directly proportional to angular velocity. These second SAW can be detected and converted to electrical signals by the receiver IDTs. Therefore, it is possible to make a gyroscope in this way. But the sensitivity of this device is significantly low, because the Coriolis Effect remains again insignificant due to the limitation on the size of metal squares. Main reason of the size limitation is the reflection of SAWs from the metal squares. If thicker metal squares are placed in the propagation path, then the

acoustic wave starts to reflect from these metal squares. As a result, this approach causes the problem of high noise level on detecting mechanisms and it is difficult to make a Z-axis gyroscope in the same piezoelectric body with this method. In conclusion, it is not possible to miniaturize these devices in order to make a 3-axis MEMS gyroscope by utilizing SAWs.

2.2   *Optical Gyroscopes*

Optical gyroscopes are based on the phenomenon of Sagnac effect, which is founded by Georges Sagnac in 1913 [17]. Sagnac used a ring interferometer to demonstrate this effect. In the ring interferometer setup, a beam of light is split and the two beams propagate in opposite directions where their trajectories form a closed loop such as triangles, squares, or rectangles. As the rotation is applied on the system, one of these two beams travels longer path than the other beam. Consequently, the interference of beams, where they arrive at starting point, has phase shift proportional to the rotation rate. This is how optical gyroscopes detect the rotation rate.

Optical gyroscopes were revealed in the 1960s, following the discovery of the laser and the development of fiber optics. Contrary to mechanical gyroscopes, optical gyroscopes have no moving parts and use the light to detect the rotation rate. Because of these characteristic reasons, optical gyroscopes have better vibration rejection performance, which is important in many industrial and military applications, than mechanical gyroscopes. That's why they have been started to be used instead of mechanical gyroscopes in air planes, missiles, and satellites as the time passed by.

2.2.1   Sagnac Effect

Sagnac's original interferometer is shown in Fig. 2.7. According to the Sagnac Effect, as the light path is rotated by a certain angular velocity, two light beams propagating in opposite directions through the closed loop complete one pass in the loop with different times. In the light path, the time difference of light beams between the exit

from a point and return to this point is directly proportional to angular velocity. In the beginning, this effect was used for sensing the rotation rate by a ring laser. The first successful test of the ring laser gyroscope was made by Macek and Davis [18]. In their experiment, an optical resonator was built by adding a laser cavity into the closed light path. This specially prepared laser cavity can emit the light in two directions. The rotated light path with a certain angular velocity causes to add different phases to propagating light beams in opposite directions. The difference of these two frequencies is directly proportional to the angular velocity. As the angular velocity is zero, there is no difference between these frequencies. This method provides a basis for optical fiber gyroscopes and ring laser gyroscopes.
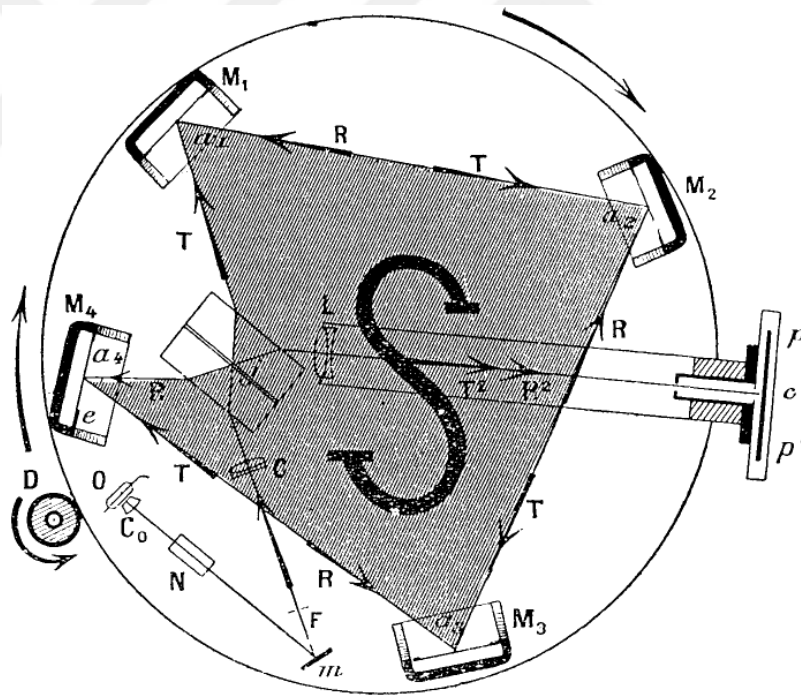
Figure 2.7: Sagnac's original interferometer [6].

The phase difference $\Delta\phi$ can be measured by using an interferometer and derived by an analytical solution where Ω is the rotating vector; t_+ and t are the traveling times of the co-rotating and counter-rotating beams respectively; R is the radius of the circular path and c is the velocity of light. The optical paths can now be calculated

for both beams:

$$ct_+ = 2\pi R + \Omega R t_+ \rightarrow t_+ = \frac{2\pi R}{c - \Omega R}$$

$$ct_- = 2\pi R - \Omega R t_- \rightarrow t_- = \frac{2\pi R}{c + \Omega R} \tag{2.11}$$

The difference in optical paths is given by:

$$\Delta L = ct_+ - ct_- = 2\pi R \left(\frac{1}{1 - \frac{\Omega R}{c}} - \frac{1}{1 + \frac{\Omega R}{c}} \right) \approx \frac{4\pi \Omega R^2}{c} \tag{2.12}$$
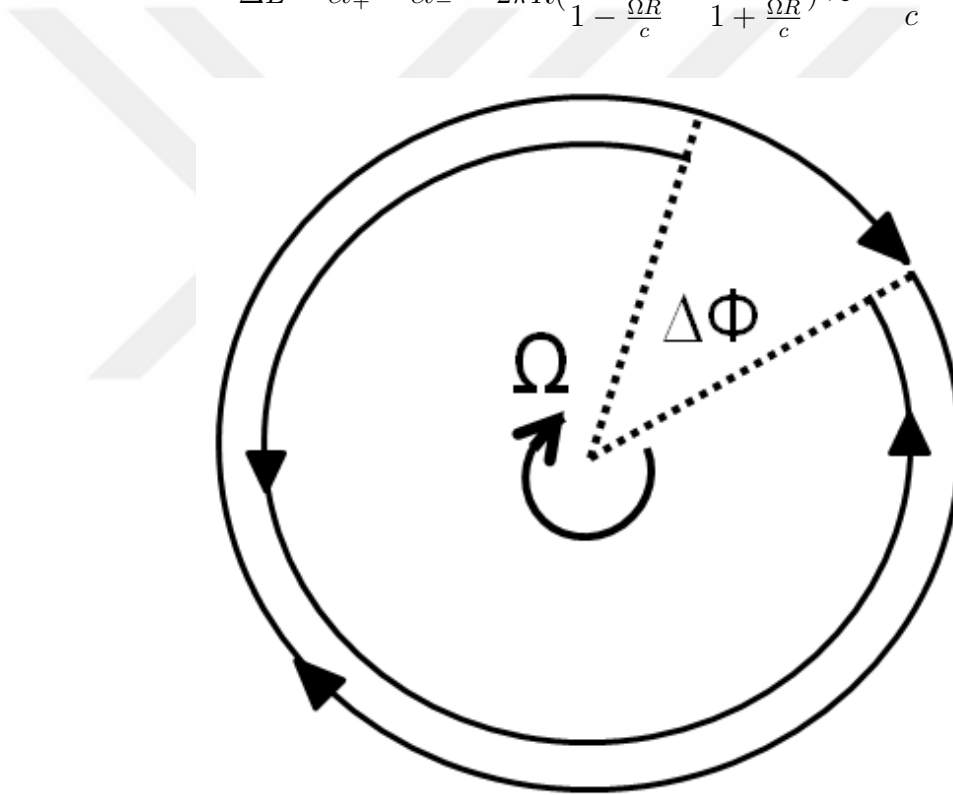
Figure 2.8: Representation of the Sagnac Effect on two light beams propagating in opposite directions.

The difference in optical paths is also shown in Fig. 2.8. In (2.12), due to the approximation which comes from $(\Omega R) \ll c$, this approach is only valid for reasonable values of Ω and R. So the phase difference between the two beams is calculated as:

$$\Delta \phi = \frac{2\pi \Delta L}{\lambda} = \frac{8\pi \Omega A}{c\lambda} \tag{2.13}$$

In (2.13), A is the area of the circular path and λ is the wavelength. This equation shows that phase difference is inversely proportional to the speed of light. The phase difference caused by the Sagnac Effect is significantly small due to the large value of the speed of light. So, the area of ring laser must be enlarged in order to increase the phase difference. But there are some practical problems to make a gyroscope by enlarging the area. For this reason, fiber optic gyroscopes were developed in order to overcome this problem [19]. In these gyroscopes, a significantly long fiber piece is wrapped around a coil and this increase the effective area. So, the Equation (2.13) can be rewritten for enclosed areas where the area vector of the closed path is given by:

$$A = \frac{1}{2} \oint r \times dr \tag{2.14}$$

Finally, we have the phase difference, which describes the Sagnac effect as the rotation vector flux which goes through the enclosed area.

$$\Delta\phi = \frac{4\omega A\Omega}{c^2} \tag{2.15}$$

2.2.2 Ring Laser Gyroscopes

Ring Laser Gyroscopes (RLGs) use the laser light in order to measure the rotation rate. The RLGs got into the market in the early 1980s [20–22]. The technology of RLG has developed to the utmost so far and they are assertive gyroscopes for the navigation systems considering their higher performance than the other gyroscopes. In RLGs, mirrors are oriented as either square or triangular boxes and laser beams travel between the mirrors by passing through the laser medium. The mixture of helium-neon(10:1) is commonly used as a laser medium, which has short coherence length and the refractive index of nearly 1.0. The laser cavity is used for increasing the Sagnac Effect due to the many times recirculation of light around the resonant

cavity. The cavity lengths of commercial helium-neon lasers are usually ranging from 15 cm to 50 cm. Furthermore, the cavity length must be tuned an integral number of wavelengths to support the lasing action, which is approximately 630 nm for helium-neon gas mixture [23,24]. The working principle of RLGs is based on two laser beams counter-propagate inside the ring cavity, as shown in Fig. 2.9. As the RLG is at rest, each laser beam propagates at the same length. So the frequency change does not occur. As the RLG rotates, the arrival times of laser beams are different from each other due to the Sagnac Effect. This impact causes the frequency difference between laser beams, which is measured by the photo detector. This frequency difference can be calculated in (2.16), where P is the perimeter of the ring.
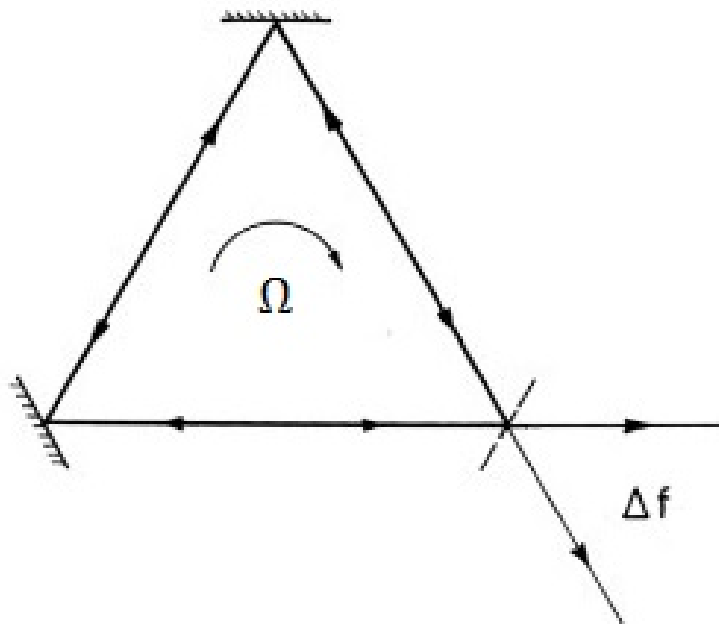
Figure 2.9: Ring laser cavity.

$$\Delta f = \frac{4A\Omega}{\lambda P} \tag{2.16}$$

The interference intensity I is modulated with the corresponding phase difference at the beat frequency Δf:

$$I = I_0(1 + \cos(\Delta\phi))$$

$$I = I_0(1 + \cos(2\pi\Delta f t)) \qquad (2.17)$$

Angular increment θ_{inc} equals to the angle regarding to one modulation period. The angular increment is simply $\lambda/2R$ where $P = 2\pi r$ and $A = \pi R^2$. Finally, the rotation rate can be obtained by counting of the beats, where Δf is proportional to Ω.

$$\theta_{inc} = \frac{\Omega}{\Delta f} = \frac{\lambda P}{4A} \qquad (2.18)$$

The mode lock-in between counter propagating beams is the common problem for RLGs. Most of the time, the backscattering of mirrors induces a coupling between oscillators to lock in same frequencies and this causes a dead zone at low rotation rate. This problem can be solved by mechanical dither system [25]. Furthermore, lifetime and reliability problems occur because of the aging of discharge electrodes and the leakage of gases.

2.2.3 Fiber Optic Gyroscopes

Fiber optic gyroscopes (FOGs) use the shift in the interference pattern of two counter-propagating light beams passing through the optical fiber in order to measure the rotation rate. This time, the light beams coming from laser diode are split into two counter propagating waves through multi-turn optical-fiber. The impact of the Sagnac effect depends on the area of closed optical path, which can be enhanced by increasing the number of turns in the coil. So, the FOGs can increase the effective area by their multi-turn optical-fiber coils in order to improve the Sagnac Effect contrary to RLGs. The first FOG was proposed by Pircher and Hepner in 1967 [26] and the first experiment was demonstrated by Vali and Shorthill in 1976 [19]. As the time

passes by, the improvement of super luminescent diode (SLD) eliminates the Rayleigh backscatter noise and drift of Kerr Effect. Also, the low-loss single-mode optical fiber, fiber polarizers, polarization maintaining couplers, solid-state light sources and detectors were developed. These all improvements provided an environment for fiber optic gyroscopes to be produced as commercial devices. Therefore, the FOGs have started to become remarkable competitor against the RLGs in the market, considering the advantages of their solid-state configuration and improved high performance over the years. The passive interferometer type of FOG (I-FOG) and the passive ring resonator FOG (R-FOG) are two different fiber optic gyroscopes regarding to their techniques to measure rotation rate by using the Sagnac Effect [27].

In the I-FOG, two light beams propagate in opposite directions through a long multi-turn optical fiber due to the development of low-loss optic fibers, which makes easier to enhance the area of closed optical path as long as possible. When an optical fiber with N loops and diameter D for each loop is used, the phase difference between the two counter propagating beams equal to:

$$\Delta\phi = \frac{8\pi NA}{\lambda c}\Omega$$
$$\Delta\phi = \frac{2\pi LD}{\lambda c}\Omega \tag{2.19}$$

Where λ is the wavelength in vacuum, D is the coil diameter, $L = N\pi D$ is the fiber coil length, $A=(\pi D^2)/4$ is the area of single fiber loop, and N is the number of loops.

The configuration of an I-FOG with two couplers and a polarizer is shown in Fig. 2.10. For this gyroscope, both light beams must travel with the same mode, therefore it is better to use a single mode fiber in order to measure the rotation rate properly. However, two counter propagating light beams can have difference between each other in their polarization states, as the gyroscope is even at rest.

26

This causes a bias fluctuation and the polarizer in Fig. 2.10 is used for solving this problem. In some cases, one coupler does not enough for these gyroscope systems due to the non-reciprocity, so it is a proper solution to fix the non-reciprocity of first-coupler by adding a second coupler [28,29]. The phase modulator creates a bias phase difference of $\pi/2$ between the two light beams in order to increase the sensitivity of the measurement, as shown in Fig. 2.11. In that case, the intensity at the detector in (2.17) changes to:

$$I = I_0(1 + \cos(\Delta\phi) - \frac{\pi}{2})$$
(2.20)
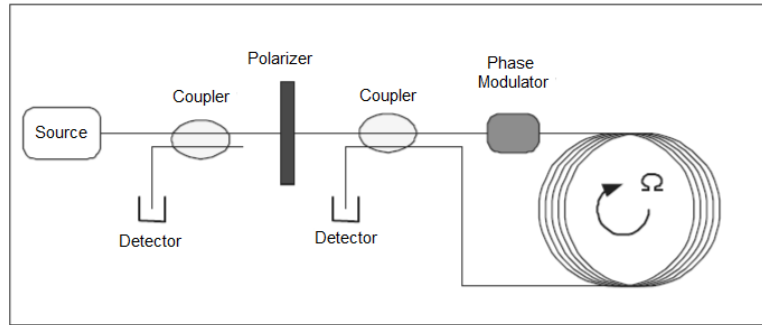
Figure 2.10: Elementary configuration of an I-FOG.
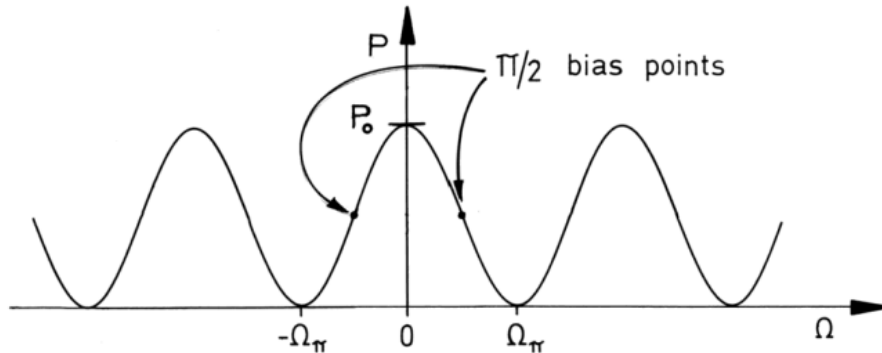
Figure 2.11: Response of an I-FOG.

In the R-FOG, a passive ring cavity is used instead of the active cavity in ring laser gyroscopes, which eliminates the problem of lock-in and Fresnel-Fizeau drag,

as shown in Fig. 2.12. The resonance frequencies of light beams propagating in opposite directions are changed as the cavity is subjected to rotational motion. The rate of change of the resonance frequency Δf is similar to (2.16) obtained in ring laser gyroscopes.

$$\Delta f = \frac{4A\Omega}{\lambda P} \tag{2.21}$$
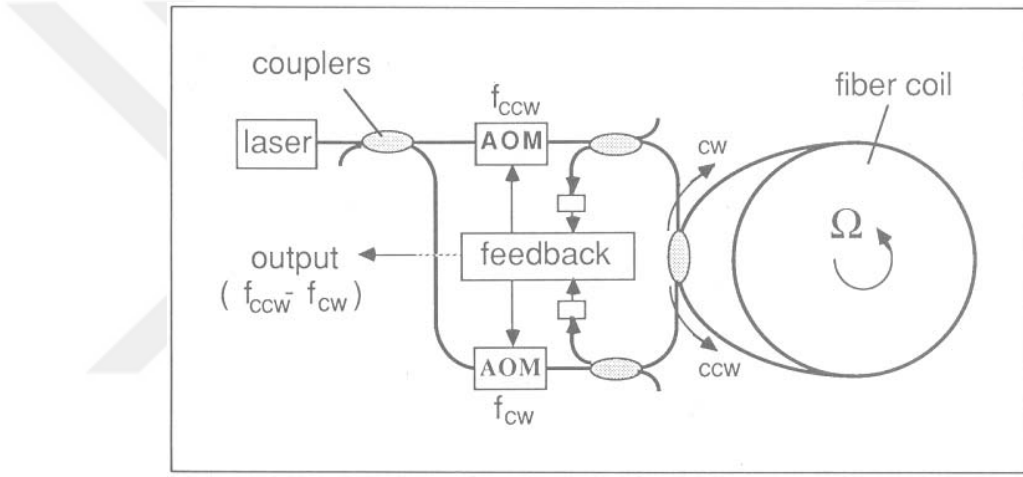
Figure 2.12: Elementary configuration of an R-FOG where the AOM is acousto-optic modulator [7].

Single mode fibers are used in these gyroscopes for increasing the sensitivity based on the number of recirculations. So, the frequency difference can be rewritten as:

$$\Delta f = \frac{4A\Omega}{n\lambda P} \Delta f = \frac{D\Omega}{n\lambda}$$

Where D is the diameter of the coil and n is the index of refraction. The potential improvement of these gyroscopes is indicated as the product of half the width of the resonance by the number N of turns compared to Sagnac interferometer.

In conclusion, it is shown that optical gyroscopes can reach higher performance than mechanical gyroscopes. However, these systems are also much bigger, expensive

and have relatively high power consumption due to using the laser diodes. This is the reason why they are not suitable for consumer markets.

2.3 Summary

Inertial sensors, which consist of accelerometer, gyroscope, compass and GPS, are widely used in navigation systems. The position and direction of a body can be detected by the combination of the proper algorithms and the measurements from inertial sensors. The key elements are accelerometers and gyroscopes for navigation systems. Besides, the compass and GPS are used for reducing the output errors of accelerometers and gyroscopes. In general, it is easy to make a high performance accelerometer. The first step for making a high performance accelerometer is to choose the proof-mass as large as possible, but making gyroscopes is more complicated. The performance of gyroscope is determined by the chosen method among the mechanical and optical gyroscopes. The high performance gyroscopes have been made by using the fiber optic method. This type of gyroscopes, which is shown in Fig. 2.13, is mostly used in navigation applications. On the other hand, MEMS gyroscopes in Fig. 2.14 are preferred for lower performance applications like smart phones. These two technologies are compared in Table 2.1.

Table 2.1: FIBER OPTIC GYROSCOPES VS. MEMS GYROSCOPES PERFORMANCE

	Optical Gyroscopes	MEMS Gyroscopes
Dimensions	10 cm x 10 cm x 10 cm	4 mm x 4 mm x 1 mm
Weight	500 gr	5 gr
Power Consumption	1 W	3 mW
Noise	$0.0001 \text{ dps}/\sqrt{Hz}$	$0.001 \text{ dps}/\sqrt{Hz}$
Angle Random Walk	$0.01 \text{ deg}/\sqrt{h}$	$0.1 \text{ deg}/\sqrt{h}$
Bias Stability	0.001 deg/h	10 deg/h
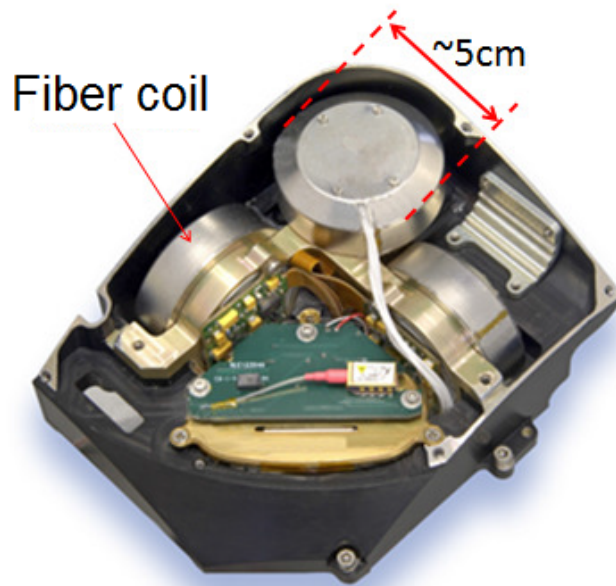
Figure 2.13: Commercial 3-axis fiber optic gyroscope. Size of the gyroscope is 15 cm x 20 cm x 6 cm.

Based on their performances, optical gyroscopes are much better than MEMS gyroscopes. On the other hand considering the size, power consumption and cost, MEMS gyroscopes are more convenient for consumer markets. In the first part of the thesis, a novel gyroscope method will be proposed, which is considered as a potential device to have not only the high performance but also the low cost specifications.
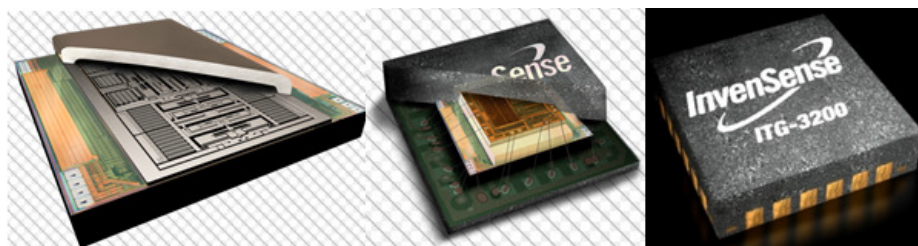
Figure 2.14: Commercial 3-axis MEMS gyroscope. In this chip, 3-axis MEMS gyroscope, is entegrated on the CMOS electronics. Size of the gyroscope is 4 mm x 4 mm x 0.9 mm.

CHAPTER III

WAVEGUIDE BASED GYROSCOPES

3.1 Design Basics

In this chapter, a cylindrical ring waveguide is presented as a novel design for mechanical gyroscopes, as shown in Fig. 3.1. Acoustic waves propagate dispersively in the cylindrical waveguides and excitation of only one mode is very important for the noise performance. In addition, the sensitivity of a gyroscope, that utilizes the acoustic waves, is inversely proportional to velocity and wavelength of the acoustic wave. Therefore, the size and operating frequency of waveguide must be chosen carefully. The modes of cylindrical waveguide are calculated numerically and the most appropriate mode is chosen considering the details in the following sections. A numerical calculation method is developed in order to calculate the dispersion curves (phase velocity vs. frequency) of free cylindrical waveguides and then, these numerical calculations are verified by finite element analysis.
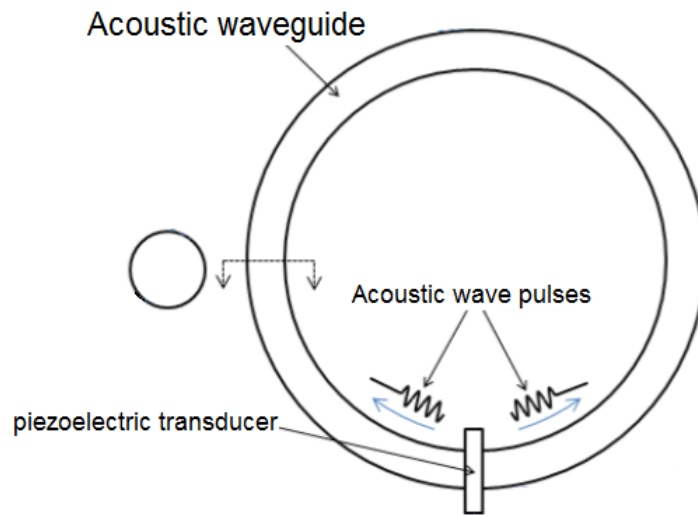
Figure 3.1: Novel Gyroscope Design.

Target specifications of the novel gyroscope are presented below:

1. Noise: 0.001 dps/$\sqrt{Hz}$

2. Angle Random Walk: 0.01 deg/$\sqrt{h}$

3. Bias Stability (Allan variance): 0.1 deg/h

4. Bandwidth > 1000 Hz

5. Temperature and external acceleration effect minimization (Temperature offset shift: 10 dps / $100°C$)

Regarding to the size and power consumption, the novel gyroscope can be remarkable competitor against the optical gyroscopes commercially in case of having the target specifications.

3.2   *Principle of Operation*

In this section, the solution of analytical model for a cylindrical waveguide is obtained. By using this analytical model, figures of the dispersion curves are shown separately for the four modes of circular rod waveguides in Fig. 3.2.
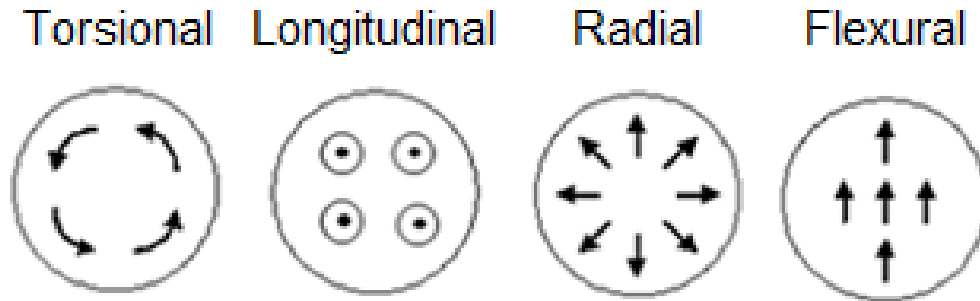
Figure 3.2: Types of the modes of circular rod waveguides.

In Fig. 3.2, it is shown that the particle motion is orthogonal to the waveguide for the flexural modes. For the radial modes, the diameter of waveguide varies as the acoustic wave propagates radially. For the torsional modes, the direction of particle

motion is around the axis of waveguide and for the longitudinal modes, it is in the same direction with the axis of waveguide. The vector particle velocity can be written in terms of a scalar (Φ) and vector potential (Ψ) in (3.1) [8].

$$v = \nabla\Phi + \nabla \times \Psi \tag{3.1}$$
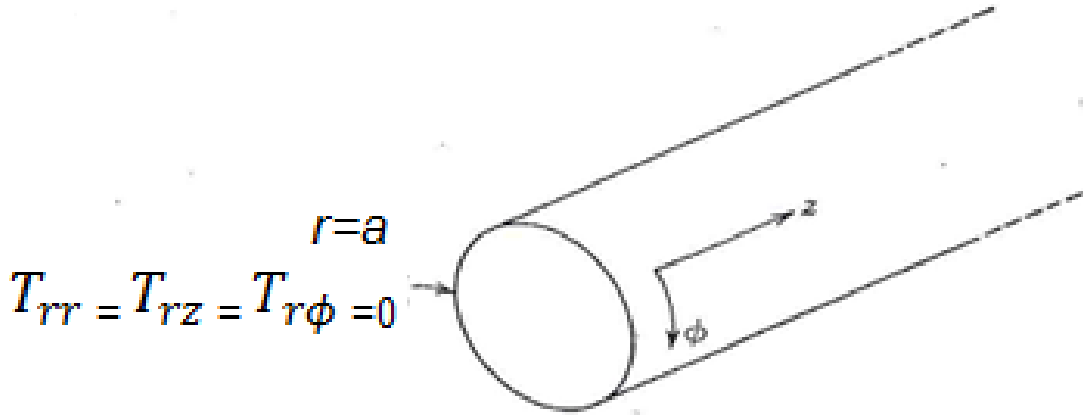
Figure 3.3: Free circular rod waveguide [8].

A circular rod waveguide is shown in Fig. 3.3. The radius of waveguide equals to a and the direction of radius equals to r. z represents the direction of axis through the waveguide and ϕ represents the angle between the radius and z in cylindrical coordinates. The boundary conditions are also shown in Fig. 3.3; the stress boundary conditions must equal to zero at the surface of circular rod waveguides.

In most general form, scalar and vector potentials must satisfy (3.2) [8].

$$\nabla^2\Phi - \frac{1}{V_l^2}\frac{\partial^2\Phi}{\partial t^2} = 0, \quad \nabla^2\Psi - \frac{1}{V_s^2}\frac{\partial^2}{\partial t^2}\Psi = 0 \tag{3.2}$$

In (3.2), V_l and V_s represent the velocities of longitudinal waves and transverse waves, respectively. Equations from (3.3) to (3.5) are the representation of (3.2) in cylindrical coordinates.

33

$$\frac{1}{r}\frac{\partial}{\partial r}\left(r\frac{\partial \Phi}{\partial r}\right) + \frac{1}{r^2}\frac{\partial^2 \Phi}{\partial \phi^2} + \frac{\partial^2 \Phi}{\partial z^2} = -\frac{\omega^2}{V_l^2}\Phi \tag{3.3}$$

$$\hat{\mathbf{r}}\left(\nabla^2\Psi_r - \frac{2}{r^2}\frac{\partial \Psi_\phi}{\partial \phi} - \frac{\Psi_r}{r^2}\right) + \hat{\phi}\left(\nabla^2\Psi_\phi + \frac{2}{r^2}\frac{\partial \Psi_r}{\partial \phi} - \frac{\Psi_\phi}{r^2}\right) + \hat{\mathbf{z}}(\nabla^2\Psi_z) = -\frac{\omega^2}{V_s^2}\Psi \tag{3.4}$$

$$\nabla^2 = \frac{1}{r}\frac{\partial}{\partial r}\left(r\frac{\partial}{\partial r}\right) + \frac{1}{r^2}\frac{\partial^2}{\partial \phi^2} + \frac{\partial^2}{\partial z^2} \tag{3.5}$$

Scalar and vector potentials must be represented in harmonic frequency as a solution of the equations from (3.3) to (3.5). The two potentials show the wave propagating in positive z direction with the wave number β.

$$\Phi_{(r,\phi)}e^{i(\omega t - \beta z)} \qquad \Psi_{(r,\phi)}e^{i(\omega t - \beta z)}$$

The standard separated variable solution to the scalar potential equation (3.2) is then:

$$\Phi = AR_p(k_{tl}r)\begin{pmatrix} \sin(p\phi) \\ \cos(p\phi) \end{pmatrix}e^{-i\beta z}$$

$$k_{tl}^2 + \beta^2 = \left(\frac{\omega}{V_l}\right)^2 \tag{3.6}$$

A is an arbitrary constant and R_p is a Bessel function. k_{tl} is the longitudinal wave number. In Fig. 3.3 the potential must remain finite at $r = 0$, and Bessel functions of the first kind are used, which is given by:

$$R_p(k_{tl}r) = J_p(k_{tl}r)$$

The vector potential equation in (3.2) has two independent divergenceless solutions:

$$\mathbf{M} = \nabla \times \hat{\mathbf{z}}\Psi \tag{3.7}$$

$$\mathbf{N} = \frac{V_s}{\omega}\nabla \times \mathbf{M} \tag{3.8}$$

Ψ in (3.7) satisfies the scalar potential equation in (3.1). Following that, Ψ has the same form as (3.6), but at this time the Bessel function is shown as below:

$$R_p(k_{ts}r) = J_p(k_{ts}r)$$

$$k_{ts}^2 + \beta^2 = (\frac{\omega}{V_s})^2$$

k_{ts} is the transverse wave number. A general solution for the vector potential is then:

$$\Psi = B\mathbf{M} + C\mathbf{N}$$

$$\mathbf{M} = \left(-\hat{\mathbf{r}}\frac{J_p(k_{ts}r)}{(k_{ts}r)}\begin{pmatrix} -\sin(p\phi) \\ \cos(p\phi) \end{pmatrix} - \hat{\phi}J_p'(k_{ts}r)\begin{pmatrix} \cos(p\phi) \\ \sin(p\phi) \end{pmatrix}\right)e^{-i\beta z} \tag{3.9}$$

$$\mathbf{N} = \left(\hat{\mathbf{r}}i\beta k_{ts}J_p'(k_{ts}r)\begin{pmatrix} -\cos(p\phi) \\ \sin(p\phi) \end{pmatrix} + \hat{\phi}\frac{i\beta p}{r}J_p(k_{ts}r)\begin{pmatrix} \sin(p\phi) \\ \cos(p\phi) \end{pmatrix}\right.$$

$$\left. -\hat{\mathbf{z}}k_{ts}^2 J_p(k_{ts}r)\begin{pmatrix} -\cos(p\phi) \\ \sin(p\phi) \end{pmatrix}\right)e^{-i\beta z}$$

Primes indicate a derivative with respect to the argument. So, the general particle velocity field in cylindrical coordinates is obtained by the substitution of scalar potential in (3.6) and vector potential in (3.9) into (3.1).

$$v_r = \left[A k_{tl} J_p'(k_{tl}r) + i\beta B J_p'(k_{ts}r) + \frac{p}{r} C J_p(k_{ts}r) \right] \begin{pmatrix} \cos(p\phi) \\ \sin(p\phi) \end{pmatrix} e^{-i\beta z}$$

$$v_\phi = \left[\frac{p}{r} A J_p(k_{tl}r) + \frac{i\beta p}{k_{ts}r} B J_p(k_{ts}r) + k_{ts} C J_p'(k_{ts}r) \right] \begin{pmatrix} -\sin(p\phi) \\ \cos(p\phi) \end{pmatrix} e^{-i\beta z} \qquad (3.10)$$

$$v_z = \left[-i\beta A J_p(k_{tl}r) - k_{ts} B J_p(k_{ts}r) \right] \begin{pmatrix} \cos(p\phi) \\ \sin(p\phi) \end{pmatrix} e^{-i\beta z}$$

The strain field in cylindrical coordinates has components:

$$
\begin{aligned}
S_{rr} &= \frac{1}{i\omega}\frac{\partial v_r}{\partial r} & S_{z\phi} &= \frac{1}{2i\omega}\left(\frac{\partial v_\phi}{\partial z} + \frac{\partial v_z}{r\partial \phi}\right) \\
S_{\phi\phi} &= \frac{1}{i\omega}\left(\frac{v_r}{r} + \frac{1}{r}\frac{\partial v_\phi}{\partial \phi}\right) & S_{rz} &= \frac{1}{2i\omega}\left(\frac{\partial v_r}{\partial z} + \frac{\partial v_z}{\partial r}\right) \\
S_{zz} &= \frac{1}{i\omega}\frac{\partial v_z}{\partial z} & S_{r\phi} &= \frac{1}{2i\omega}\left(\frac{1}{r}\frac{\partial v_r}{\partial \phi} + \frac{\partial v_\phi}{\partial r} - \frac{v_\phi}{r}\right)
\end{aligned}
\qquad (3.11)
$$

and these are converted to abbreviated subscript notation by the relations:

$$
\begin{aligned}
S_1 &= S_{rr} & S_4 &= 2S_{z\phi} \\
S_2 &= S_{\phi\phi} & S_5 &= 2S_{rz} \\
S_3 &= S_{zz} & S_6 &= 2S_{r\phi}
\end{aligned}
\qquad (3.12)
$$

Stress components are calculated from (3.11),(3.12) and (3.13). The boundary conditions are given by (3.14); they equal to zero at the surface of waveguide, as shown in Fig. 3.3.

$$\mathbf{T} = \mathbf{c} : \mathbf{S} \tag{3.13}$$

$$T_{rr} = T_1 = 0$$

$$T_{rz} = T_5 = 0 \tag{3.14}$$

$$T_{r\phi} = T_6 = 0$$

These boundary conditions must be applied at $r = a$. In the case of an isotropic medium, the stiffness matrix has the form in cylindrical coordinates as it does in cartesian coordinates and the boundary equations (3.14) take the form:

$$T_1 = \frac{1}{i\omega}\left(c_{11}\frac{\partial v_r}{\partial r} + c_{12}\left(\frac{v_r}{r} + \frac{1}{r}\frac{\partial v_\phi}{\partial \phi}\right) + c_{12}\frac{\partial v_z}{\partial z}\right) = 0$$

$$T_5 = \frac{1}{i\omega}c_{44}\left(\frac{\partial v_r}{\partial z} + \frac{\partial v_z}{\partial r}\right) = 0 \tag{3.15}$$

$$T_6 = \frac{1}{i\omega}c_{44}\left(\frac{1}{r}\frac{\partial v_r}{\partial \phi} + \frac{\partial v_\phi}{\partial r} - \frac{v_\phi}{r}\right) = 0$$

Substitution of the particle velocity field in (3.10) leads to the three equations in A, B, C.

$$
\begin{bmatrix}
\left(\begin{array}{c} -c_{12}(k_{tl}^2 + \beta^2)J_p(k_{tl}a) \\ +2c_{44}k_{tl}^2 J_p''(k_{tl}a) \end{array}\right) & 2c_{44}i\beta k_{ts}J_p''(k_{ts}a) & \left(\begin{array}{c} \dfrac{2c_{44}p}{a}\left(\begin{array}{c} k_{ts}J_p'(k_{ts}a) \\ -\dfrac{1}{a}J_p(k_{ts}a) \end{array}\right) \\ +\dfrac{2c_{12}p}{a}k_{ts}J_p'(k_{ts}a) \end{array}\right) \\[4em]
2i\beta k_{tl}J_p'(k_{tl}a) & (k_{ts}^2 - \beta^2)J_p'(k_{ts}a) & \dfrac{i\beta p}{a}J_p(k_{ts}a) \\[2em]
\dfrac{2p}{a}\left(\begin{array}{c} k_{tl}J_p'(k_{tl}a) \\ -\dfrac{1}{a}J_p(k_{tl}a) \end{array}\right) & \dfrac{2i\beta p}{k_{ts}a}\left(\begin{array}{c} k_{ts}J_p'(k_{ts}a) \\ -\dfrac{1}{a}J_p(k_{ts}a) \end{array}\right) & \left(\begin{array}{c} k_{ts}^2 J_p(k_{ts}a) \\ +\dfrac{2k_{ts}}{a}J_p'(k_{ts}a) \end{array}\right)
\end{bmatrix}
\begin{bmatrix} A \\[4em] B \\[3em] C \end{bmatrix} = 0 \quad (3.16)
$$

The characteristic equation is obtained by setting the determinant of these equations equal to zero. Solving this problem in the general case is a very difficult task, but the dispersion curves of modes shown in Fig. 3.2 can be calculated separately

by this method based on their mode shapes. In the beginning, the dispersion curves of torsional modes are calculated and then, the phase velocities of radial and longitudinal modes are calculated by using the same method. In the end, the complex calculations are expanded to obtain the dispersion curves for flexural modes, which are considered as the main mode for the novel design.

For torsional modes, C is decoupled from A and B in (3.16) and $p = 0$. Under these conditions, the corresponding characteristic equation is:

$$\left(k_{ts}^2 J_p(k_{ts}a) + \frac{2k_{ts}}{a} J_p'(k_{ts}a)\right) \times \begin{vmatrix} \left(\begin{array}{c} -c_{12}(k_{tl}^2 + \beta^2)J_p(k_{tl}a) \\ +2c_{44}k_{tl}^2 J_p''(k_{tl}a) \end{array}\right) & 2c_{44}i\beta k_{ts}J_p''(k_{ts}a) \\ 2i\beta k_{tl}J_p'(k_{tl}a) & (k_{ts}^2 - \beta^2)J_p'(k_{ts}a) \end{vmatrix} = 0 \quad (3.17)$$

In (3.16), the constant C can have a non-vanishing value only when:

$$k_{ts}^2 J_p(k_{ts}a) + \frac{2k_{ts}}{a} J_p'(k_{ts}a) = 0 \quad (3.18)$$

Since A and B can be set independently equal to zero, this gives a set of solutions from (3.10).

$$v_r = v_z = 0$$
$$v_\phi = Ck_{ts}J_0(k_{ts}r)e^{-i\beta z} \quad (3.19)$$
$$= -Ck_{ts}J_1(k_{ts}r)e^{-i\beta z}$$

These are the torsional modes where the particle velocity is entirely azimuthal, as shown in Fig. 3.4; there is no particle motion radially and in the z direction. The particle motion is zero at the origin and alternates in sign with increasing r. The representation of torsional modes is assigned as T_{0q} where $p = 0$ and q represents the

solution of (3.18) in the order of increasing k_{ts}. For instance, $k_t s$ equals to zero for $q = 0$ at T_{00} and v_ϕ approximately equals to r. In this case, every section of the rod rotates around the axis of waveguide.
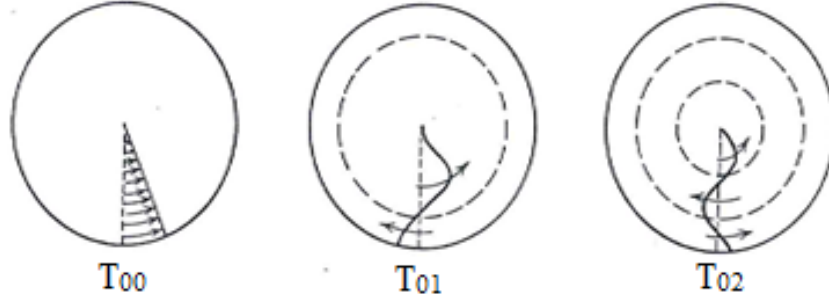
Figure 3.4: Particle velocity distributions for the three lowest order members of the torsional mode family T_{0q} [8].

In Fig. 3.5, dispersion curves of an example rod design are obtained for the lowest 4 torsional modes by solving the (3.18). Material of the example rod design is quartz and the diameter equals to 125 μm. Other dispersion curves are also going to be obtained for this design.
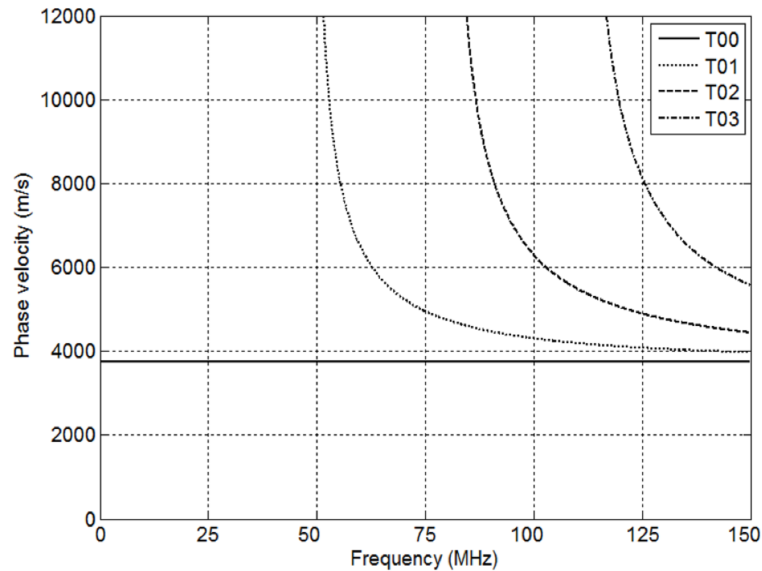
Figure 3.5: Dispersion curves of torsional modes (T_{0q}).

Other two modes are radial and longitudinal modes for the case of $p = 0$. These two modes are obtained by equating the 2x2 determinant in (3.17) to zero. This gives the Pochhammer frequency equation. At this time, C must be zero; A and B are non-vanishing. For the special case $\beta = 0$, solutions are simple, because the determinant becomes diagonal.

$$A = C = 0; \quad J_1(k_{ts}a) = 0 \tag{3.20}$$

$$B = C = 0; \quad -c_{12}J_0(k_{tl}a) + 2c_{44}J_0''(k_{tl}a) = 0 \tag{3.21}$$

(3.20) gives $v_r = v_\phi = 0$ and (3.21) gives $v_z = v_\phi = 0$ from (3.10). In these cases, the particle motion is entirely axial in (3.20) and entirely radial in (3.21), as shown in Fig. 3.6.
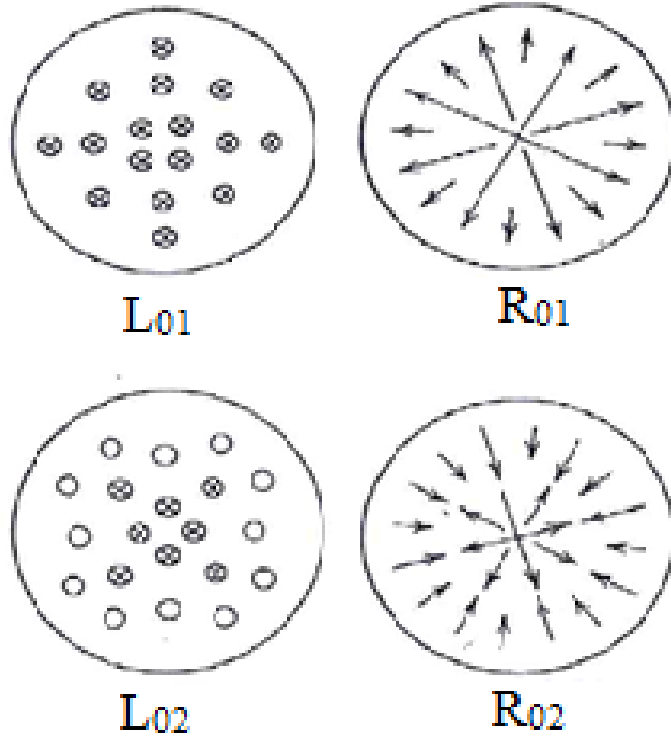
Figure 3.6: Schematic particle displacement patterns for the lowest order dilatational modes of a circular rod at $\beta = 0$ [8].
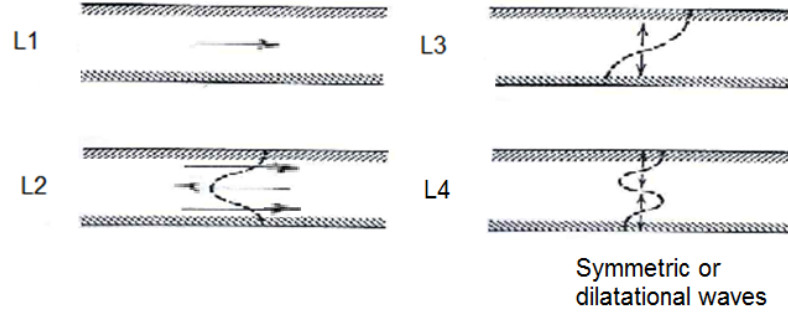
Figure 3.7: Distribution of the particle velocity field for the four lowest dilatational modes of Lamb wave where $\beta = 0$ [8].

C is still zero, as these two motions are coupled ($\beta \neq 0$). Therefore, the particles move in radial planes. These modes are called generally dilatational modes. In Fig. 3.7, dilatational modes resembles with the symmetric Lamb modes of free plate. The particle velocity fields have a radial component, which does not vary azimuthally. The free boundary alternately dilates and contracts. Thus, the dilatational modes can be subclassified as L_{0q} and R_{0q} according to their motions, as shown in Fig. 3.6.

In Fig. 3.8 and Fig. 3.9, dispersion curves are shown for the lowest 3 longitudinal and radial modes of the example rod design by solving (3.20) and (3.21), respectively. These two modes were obtained separately in order to make easier the calculation of dilatational modes.

The azimuthally symmetric modes have been analyzed so far. Now, the dispersion curves of flexural modes are going to be obtained. Indeed, the flexural modes (azimuthally not-symmetric modes) are considered as the main mode, because the Coriolis force affects the flexural mode as the rotation is applied around the axis. However, other modes are not efficiently affected by the Coriolis force. Either, the particle motion is not orthogonal to the rotation axis or the components of particle motion orthogonal to rotation axis counteract each other for other modes (radial, torsional, longitudinal). This is the reason why the flexural modes are considered in the novel design.
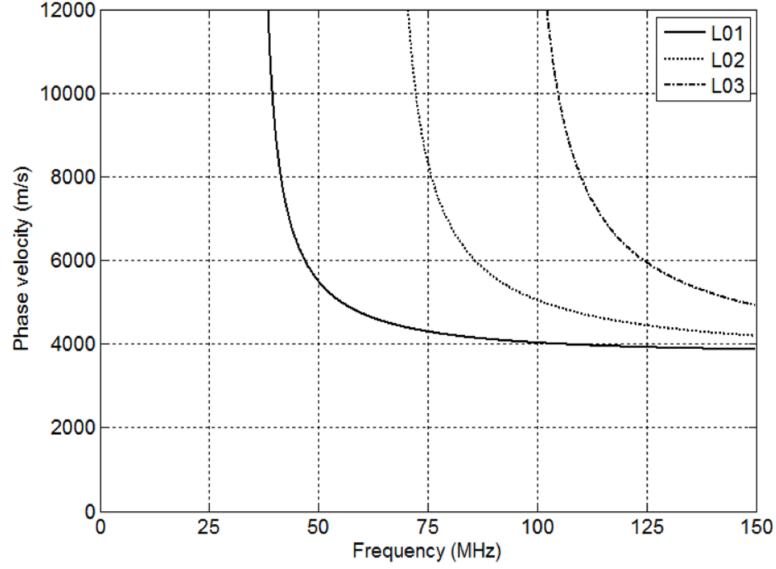
Figure 3.8: Dispersion curves of longitudinal waves (L_{0q}).
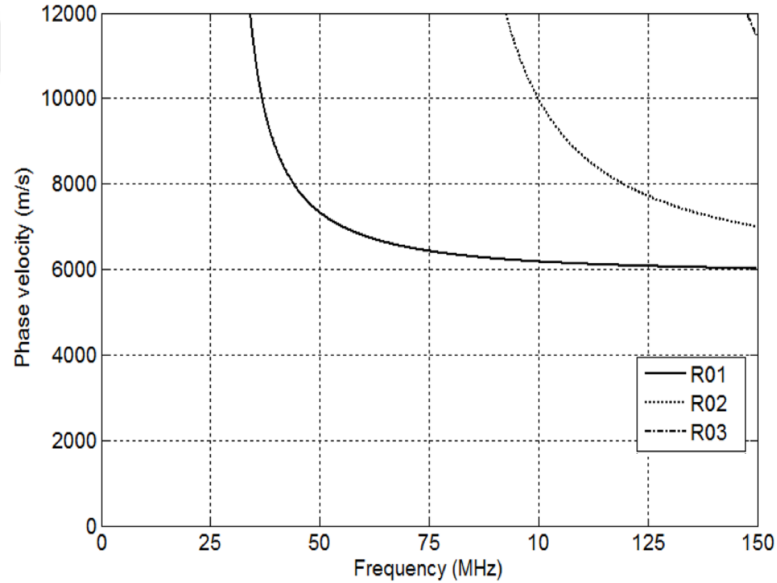
Figure 3.9: Dispersion curves of radial waves (R_{0q}).

In the case of $p = 1$, dispersion curves of flexural modes can be calculated. So, as the 3x3 matrix in (3.16) is solved for $p = 1$, dispersion curves of flexural modes for the example rod design are obtained as shown in Fig. 3.10. The velocity of first flexural mode starts from the 0 and it reaches the shear velocity of material as the frequency increases. Only the first mode is supported until 20 MHz for a 125 micron

42

quartz rod and other modes start to be supported by the waveguide as the frequency increases. As a conclusion of the analyses, our aim is to make a gyroscope, which utilizes the first flexural mode.
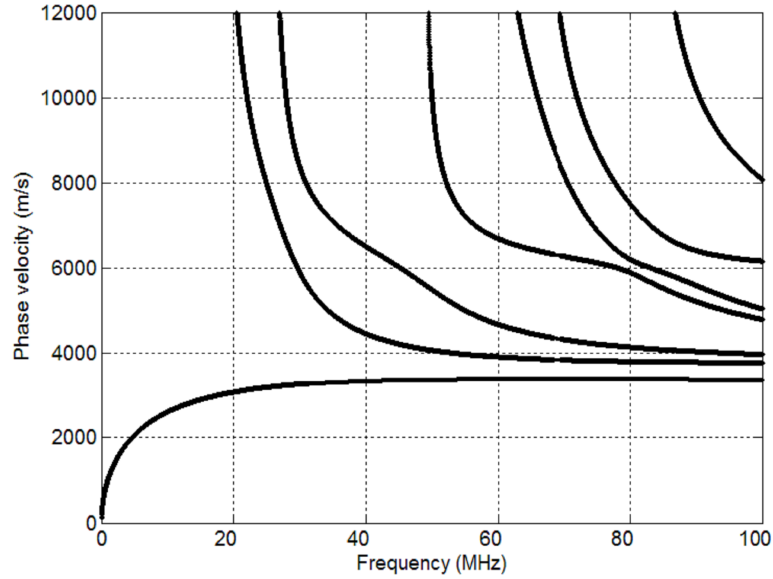
Figure 3.10: Dispersion curves of flexural waves (F_{0q}).

3.3 Simulation and Results

The sensitivity of gyroscopes is inversely proportional to the frequency, so it is better to work at low frequencies for gyroscopes. On the other hand, the phase shift of a wave in the acoustic waveguide is going to be decrease due to increasing wavelength as the frequency decreases. Therefore, it is necessary to solve an optimization problem for this condition. The phase velocity of flexural modes is always lower than others considering their first modes and accordingly the wavelengths of flexural modes are always smaller than others. In this case, it is possible to make a more sensitive gyroscope by utilizing the first flexural mode compared to other modes. That is why the first flexural mode is considered in the next ANSYS model for the novel design.

In Fig. 3.11, the 3-D model of a quartz circular rod, where the length is 5 cm and the diameter is 125 μm, is designed in ANSYS to make the calculation of wave
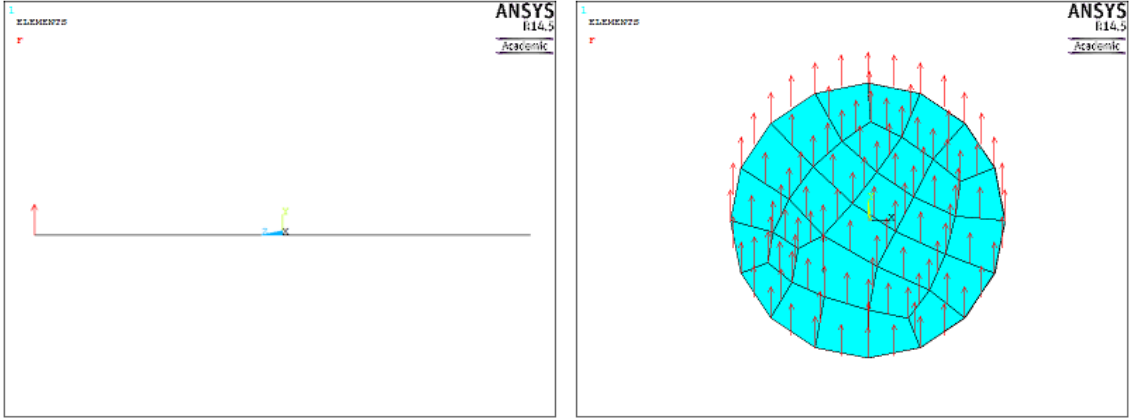
Figure 3.11: ANSYS model of the example rod design.

propagation. (Quartz: Young's modulus = 86 GPa, Poisson ratio = 0.16, density = 2650 kg/m^3). The length of waveguide is indicated as the length of 10 wavelengths. The important point is; as the rod is excited from one point, the reflection of acoustic waves from the other point must be canceled out as far as possible. So, another rod is added at the end of 5 cm rod, but this time it is provided that the wave propagates in this second section with loss and is totally absorbed before reaching at the end. The mechanical impedance is almost matched between the first and second rod with this method, so the calculation of wave propagation can be performed with an insignificant reflection.
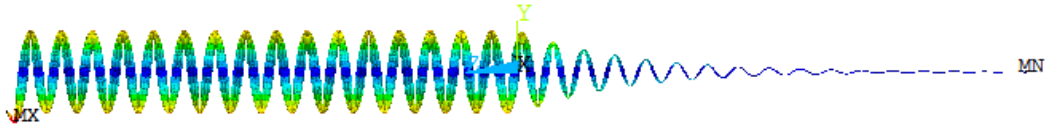
Figure 3.12: Harmonic analysis of the example rod design.

The frequency of the example rod design is operated at 100 kHz in the harmonic analysis and the first flexural mode is excited by applying 10^{-3} N in the y direction, as shown in Fig. 3.11. Wave motion of the first flexural mode is shown in Fig. 3.12. As mentioned above, the most important point for the analysis of an acoustic wave is

44
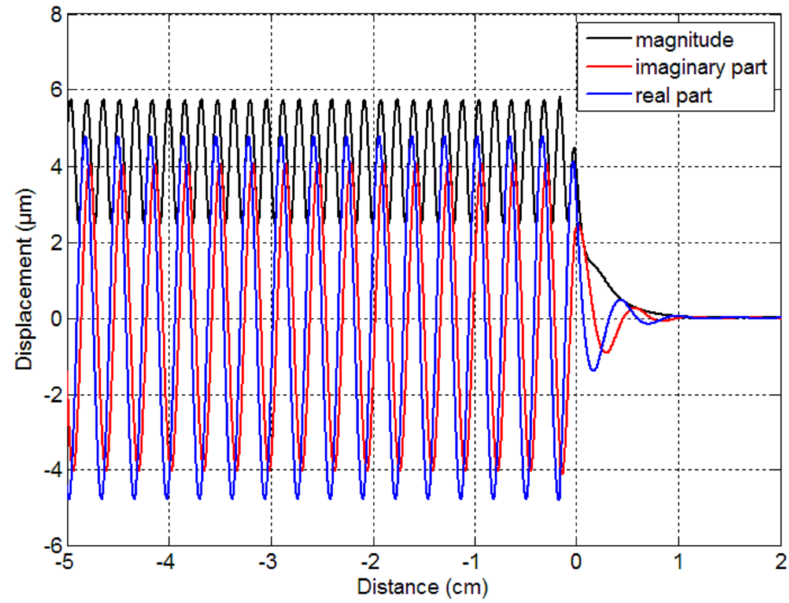
Figure 3.13: Displacement and reflection of the acoustic wave along the y axis. When the loss coefficient in the lossy part was not chosen appropriately (Damping ratio=5x10^{-6}).
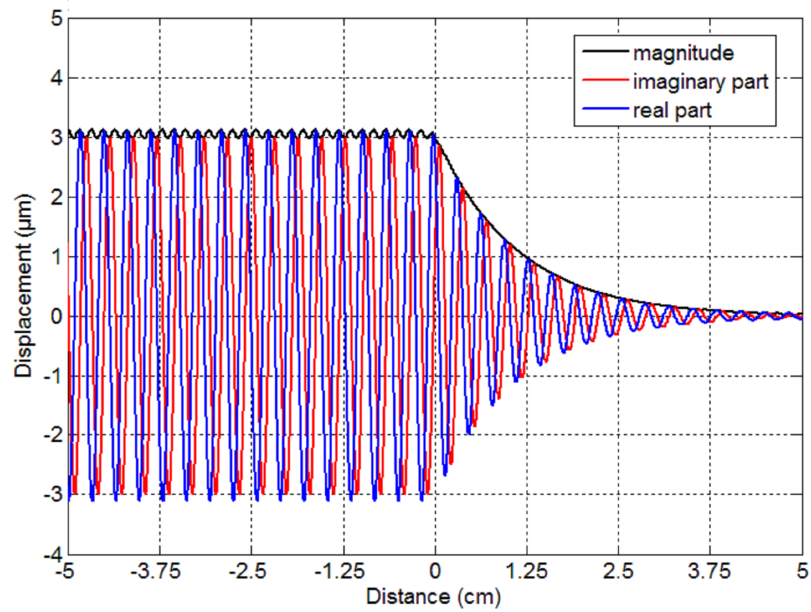
Figure 3.14: Displacement of the acoustic wave along the y axis. From 0 to 5 cm, the magnitude of standing wave is significantly small (black the magnitude), this indicates that the reflection coming from the interface point is small (Damping ratio=5x10^{-7}).

to make the reflection from end of the waveguide as low as possible. The process of absorbing acoustic wave must be performed in the length of 10 or 15 wavelengths. For this reason, we designed the first 5 cm section as lossless and introduced all loss for following 5 cm section. In Fig. 3.13 and Fig. 3.14, the wave motion is shown for two different damping ratios. Damping ratio is too much in Fig. 3.13, therefore reflections generate undesired standing waves in the first section of rod. If the reflections had been reduced to zero, the magnitude would have become stable in Fig. 3.13, where the black line shows magnitude of the wave. On the other hand, this requirement was fulfilled and the process of absorbing acoustic wave was performed successfully in Fig. 3.14. Furthermore, it is indicated from Fig. 3.14 that the wavelength of acoustic wave is 0.3125 cm and the velocity of this wave is 312.5 m/s at 100 kHz. This velocity calculation verifies almost the corresponding phase velocity in Fig. 3.15. It shows only the dispersion curve of the first flexural mode among other modes in Fig. 3.10. At the end, this verification proves that our method and math are true for the calculation of Fig. 3.10.
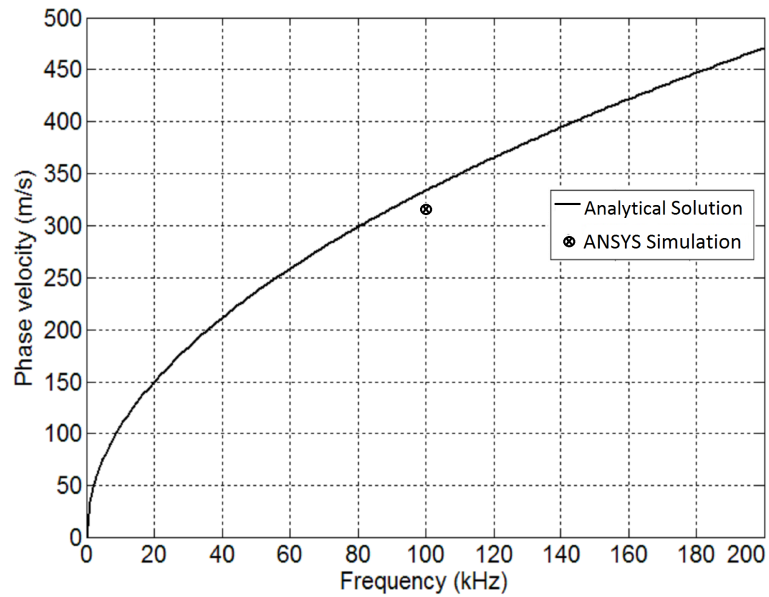
Figure 3.15: Dispersion curve of the first flexural mode of example design.

Then, the calculations for ring waveguides are performed in ANSYS. A ring waveguide from a circular rod is designed, as shown in Fig. 3.16.
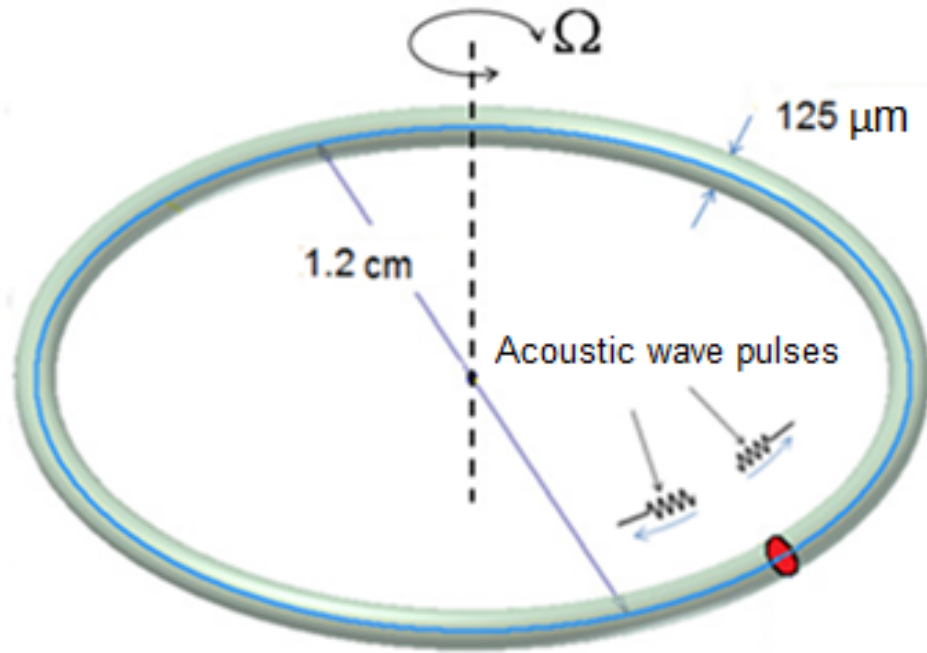
Figure 3.16: Design of the ring waveguide from a circular rod.

After analyzing the flexural modes of a circular rod, a ring waveguide is made as the main design in order to investigate its flexural modes, as shown in Fig. 3.16. The ring waveguide is designed by rounding and attaching from its two ends of the circular rod, which is analyzed in previous section. But this time, it is assumed that the whole body is lossless. The modal analysis is used to analyze flexural modes of the ring waveguide. Two conjugate modes, where the resonant frequency is at 100 KHz (14th mode), are shown in Fig. 3.17. Mode 2 is 45° degree rotated version of Mode 1 and they are orthogonal to each other. In Fig. 3.18, the frequencies of two conjugate flexural modes at around 100 kHz (14th mode) shift, as the rotation is applied around the axis going through the middle of ring waveguide.
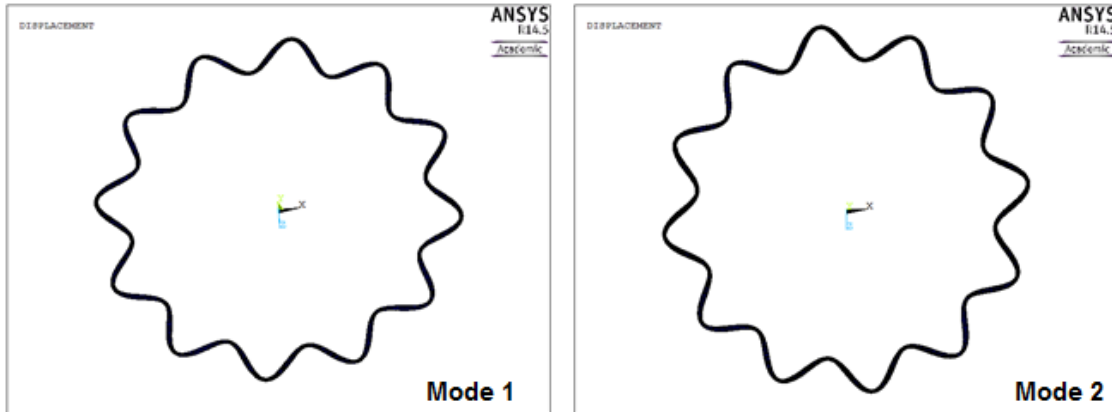
Figure 3.17: Conjugate flexural modes of the ring waveguide at around 100 kHz.
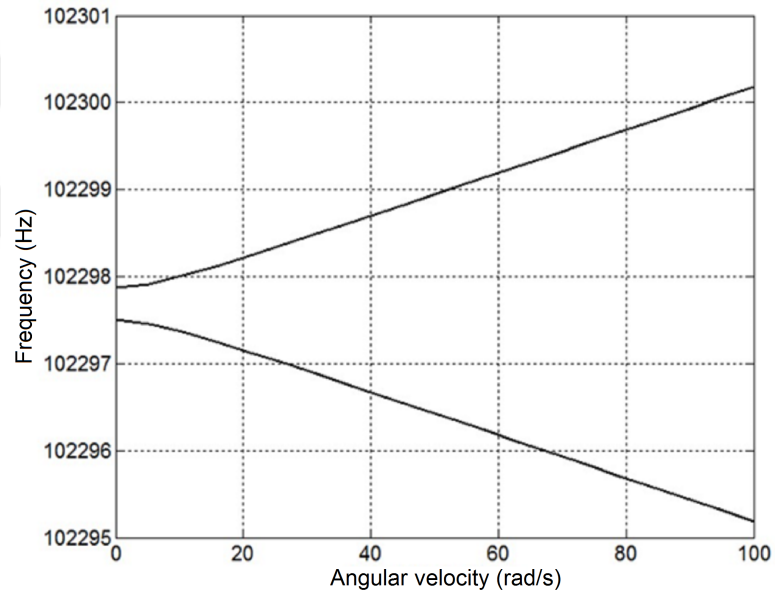
Figure 3.18: Resonant frequencies of the two conjugate flexural modes.

As a result of the analyses in ANSYS, what's discovered is that the frequency shift occurs because of the coupling between two flexural conjugate modes. When the system is at rest, there is no frequency shift. As the rotation rate is increased, two conjugate modes are coupled due to Coriolis and centrifugal forces. One of the resonance frequencies starts to increase and other one decreases. Indeed, our aim was to analyze the wave modes at higher frequencies (10-100 MHz), but it was observed that frequencies of flexural resonances of the ring waveguide shifted by the rotation

rate unexpectedly. Besides, the coupling effect can cause serious linearity problems for the all commercial mechanical gyroscopes; therefore we will analyze the well-known gyroscope systems whether this coupling affects their drive and sense resonances in the next chapter.

CHAPTER IV

ANALYSIS OF VIBRATORY GYROSCOPES

MEMS gyroscopes are finding wide range of applications in automotive and consumer electronics. In automotive they are being used for vehicle stability control, roll over detection and advanced navigation systems. Consumer electronics applications include gesture recognition for smart phones and tablets, input devices, image stabilization for cameras and camcorders [30–33]. These markets are demanding lower cost, smaller size, low power and high performance. Especially recently emerged applications, devices such as GPS assisted personal navigation (PND) and location-based services (LBS) for cell phones require low noise, high stability and high linearity [34]. As a result, more accurate analytical and numerical models are required.

In previous chapter, the resonant frequency shift of a ring waveguide was discovered due to the Coriolis force. The resonant frequency shift can cause the linearity problem in mechanical gyroscope systems. Therefore, in this chapter vibratory gyroscopes are analyzed in order to find out whether their drive and sense systems are also affected by the Coriolis Effect. A typical vibratory gyroscope is composed of a drive system and a sense system. In the drive system, a periodic oscillation of a proof mass is maintained at a constant amplitude whereas in the sense system orthogonal vibrations of the proof mass to the drive mode are detected. As the input rate is increased, driven proof mass starts to vibrate in the sense direction due to the Coriolis force. As a result, drive and sense systems are coupled together through the Coriolis force. In most of the previous work coupling between drive and sense systems have been ignored [1] and [35]. In this chapter we performed rigorous analyses of gyro systems to include this coupling and centrifugal force. We studied both 2-DOF

and Multi-DOF vibratory gyroscopes that are commonly used. These gyros usually employ multiple proof masses coupled by a network of spring systems [33, 36–38]. Based on our analyses we observed that, drive and sense resonant frequencies shift as a rotation rate is applied to a gyro system.

In macro-scale, the frequency shift due to gyroscopic effect has been observed and analyzed in a rotor system which is composed of a cylindrical rod with a disk in the middle [39]. In one of the modes which is called wobbling, the rod moves in its second flexural mode and the disk moves out of plane. The frequency of this mode shifts with the rotation of the rotor due to the gyroscopic effect which changes the stiffness of the system. In [40], in plane and out of plane modes of rings are studied to see the effect of Coriolis coupling with the applied angular velocity.

In micro-scale, the frequency shift due to gyroscopic effect has been investigated for micro rectangular beams [41]. For cantilever beams, two flexural modes moving orthogonal to each other are excited to form two oscillators. Each oscillator works at the resonant frequency of the corresponding mode. The resonant frequencies of the two modes of vibration couple with the applied angular velocity along the cantilever length due to the Coriolis Effect and this coupling causes the resonant frequency shift. It is claimed that this shift between two modes can be used for designing a vibratory gyroscope based on frequency detection.

In this chapter, we extent the work presented in [41] and demonstrate the application of method for 2 DOF and multi-DOF systems. In order to identify the frequency shift, analytical solutions were performed for simple gyro systems and numerical tools were used for complex gyro systems.

4.1   *Analysis of Simple Harmonic Oscillators*

Fig. 4.1 shows a simple harmonic oscillator. We assumed the rotation axis coincides with the proof mass. Neglecting Coriolis force the equation of motion of the linear

harmonic oscillator is given in (4.1) with a proof-mass of m, a spring constant of k_x, and a damping coefficient of c_x.
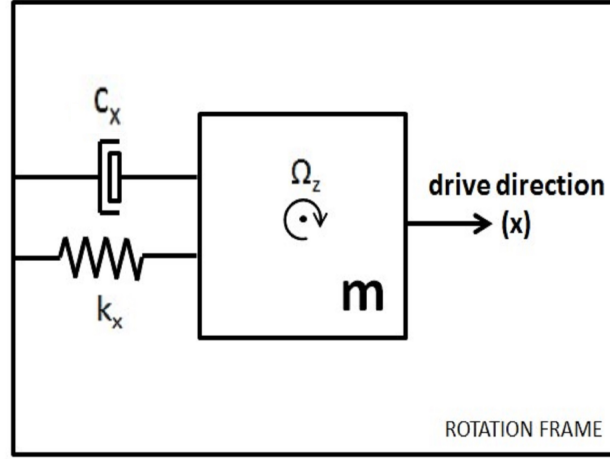
Figure 4.1: Mass-spring-damper system of the linear harmonic oscillator.

$$m\ddot{x} + c_x\dot{x} + (k_x - m\Omega_z^2)x = 0 \tag{4.1}$$

Resonant frequencies of the system is obtained from (4.1) while $\Omega_z \neq 0$.

$$w_{SHO} = \sqrt{\left(\frac{k_x}{m} - \Omega_z^2\right) - \frac{c_x^2}{4m^2}} \tag{4.2}$$

For a bulk micro-machined prototype oscillator the spring constant is 40 N/m and its proof mass is $1\mathrm{x}10^{-6}$ kg. It is clearly seen that the resonant frequency of simple harmonic oscillator decreases due to centrifugal force since rotation is applied to the system in Fig. 4.2.

In this chapter, we start with the analysis of 2-DOF mode matched gyroscopes. In a typical vibratory gyroscope, the proof mass is vibrated at its resonant frequency through a closed loop system. When the gyroscope rotates there are two forces applied to the proof mass; 1. Coriolis force, 2. Centrifugal force. The effect of the centrifugal force has been studied previously. We repeated the analysis of a simple harmonic
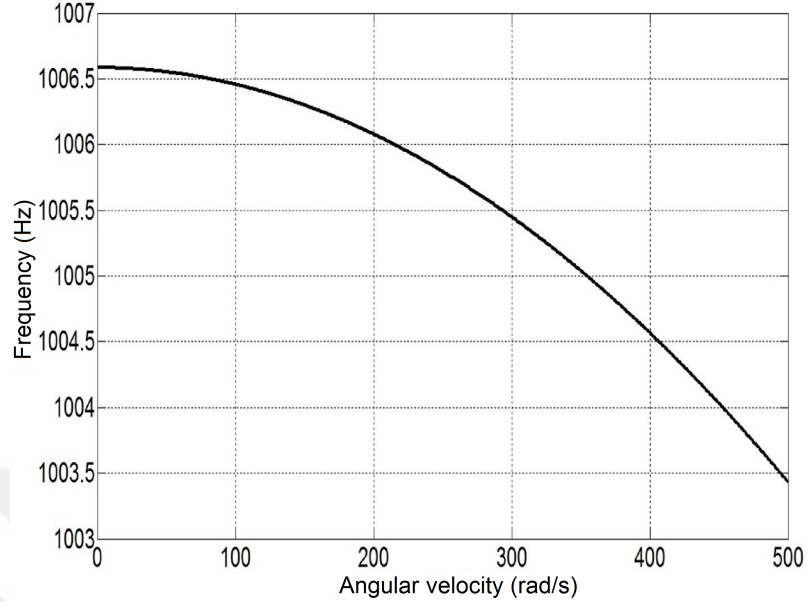
Figure 4.2: Resonant frequencies of the linear harmonic oscillator while $\Omega_z \neq 0$.

oscillator (SHO) experiencing only centrifugal force as shown in above analysis. For centrifugal force, the location of the rotation axis is important. As the radius of rotation increases the total DC force on the proof mass increases. However, the AC force that is due to the centrifugal force is only dependent on the amplitude of the proof mass vibration. Therefore, the resonant frequency shift is independent of the DC force as shown in above analysis. Based on this, in our analyses we assumed that the rotation is applied at the center of the proof mass throughout the text without loss of generality.

4.2 Drive and Sense Mode Resonance Shift by Coriolis Force

4.2.1 Linear 2-DOF Vibratory Gyroscopes

A generic z-axis gyroscope which is used to detect rotation along z-axis is shown in Fig. 4.3. The proof mass vibrates in the drive direction (x) and the sense system detects the vibration of the proof mass in the sense direction (y) due to Coriolis force as the input rate is applied. To establish the correct equation of motion for the

53

proof mass, one needs to consider both the Coriolis force and the centrifugal force. We assumed the rotation axis goes through the point mass m as explained above. According to [1], if the angular input rate is constant then the equation of motion is formed in (4.3) for linear 2-DOF vibratory gyroscopes in a rotating reference frame. $2\Omega_z m\dot{y}$ and $2\Omega_z m\dot{x}$ denote Coriolis acceleration and $xm\Omega_z^2$ and $ym\Omega_z^2$ are centripetal accelerations.
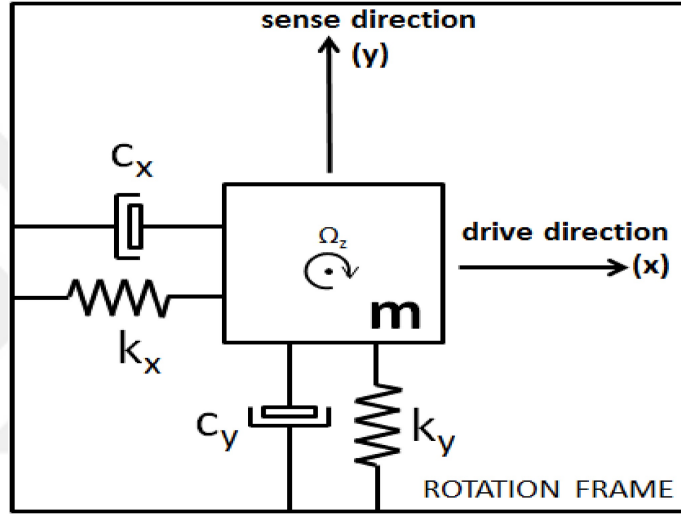
Figure 4.3: Mass-spring-damper system of the 2-DOF Vibratory Gyroscope. Rotation axis is going through the point mass.

$$m\ddot{x} + c_x\dot{x} + k_x x = -2\Omega_z m\dot{y} + xm\Omega_z^2$$
$$m\ddot{y} + c_y\dot{y} + k_y y = -2\Omega_z m\dot{x} + ym\Omega_z^2 \tag{4.3}$$

The equation of motion of the gyroscope given in (4.3) can be written in the state-space notation where one variable (X) can be used to represent amplitudes of drive and sense mode:

$$\dot{X} = AX + B$$
$$Y = CX + D \tag{4.4}$$

54

where

$$X = \begin{bmatrix} x \\ y \\ \dot{x} \\ \dot{y} \end{bmatrix} \tag{4.5}$$

$$A = \begin{bmatrix} 0 & 0 & 1 & 0 \\ 0 & 0 & 0 & 1 \\ \frac{-k_x}{m} + \Omega_z^2 & 0 & \frac{-c_x}{m} & -2\Omega_z \\ 0 & \frac{-k_y}{m} + \Omega_z^2 & 2\Omega_z & \frac{-c_y}{m} \end{bmatrix} \tag{4.6}$$

$$B = \begin{bmatrix} 0 \\ 0 \\ \frac{F_0}{m} \\ 0 \end{bmatrix}, C = \begin{bmatrix} 1 & 0 & 0 & 0 \\ 0 & 1 & 0 & 0 \end{bmatrix}, D = 0 \tag{4.7}$$

In general A matrix has three parts as shown in Equation (4.8)

$$A = \begin{bmatrix} 0 & M \\ K & C \end{bmatrix} \tag{4.8}$$

M denotes the mass part for linear and the moment of inertia part for torsional systems, respectively. K denotes the stiffness part (linear or rotational) and C denotes the damping part. According to (4.6) damping part of A matrix consists of Coriolis accelerations and the damping coefficients of the system and the spring part of the A matrix consists of centripetal acceleration and the spring constants of the system. Mass part of A matrix consists of only one proof mass where all springs and dampers are connected for a 2 DOF system.

One can calculate the resonant frequencies of the system by finding the Eigen values of A matrix. There are 2 sets of Eigen values corresponding to drive mode

55

Table 4.1: 3 DESIGNS FOR LINEAR 2-DOF VIBRATORY GYROSCOPES AND THEIR RESONANT FREQUENCIES WHEN $\Omega_z = 0$.

Designs	k_x (N/m)	k_y (N/m)	f_{drive} (kHz)	f_{sense} (kHz)
Design 1	1	1	35.59	35.59
Design 2	1.0005	0.9995	35.60	35.58
Design 3	1.001	0.999	35.61	35.57

and sense mode for 4x4 A matrix. Each set consists of two complex conjugate Eigen values. The imaginary parts of the Eigen values are the resonant frequencies and the real parts determine the damping factor for the corresponding system.

We calculated the Eigen frequencies of three designs with different uncoupled resonances that are summarized in Table 4.1. In a typical mode matched gyro, drive and sense resonant frequencies are very close to each other. For all the designs we assumed the spring constants of drive and sense systems are around 1 N/m and the proof mass is exactly 20×10^{-12} kg. These values are consistent with typical MEMS gyroscopes. In design 1, the spring constants of the drive and sense oscillators are equal to each other (1 N/m) therefore the resonant frequencies match each other. For the second and third design spring constants are slightly different resulting in slight mismatches in the resonances. We plotted Eigen values to depict how resonant frequencies for a linear 2-DOF vibratory gyroscopes shift for various input rates in Fig. 4.4 and 4.5. In Fig. 4.4, we assumed same Q_s for the drive and the sense systems whereas in Fig. 4.5, Q_s are different.

For design 1 (mode matched design), when the input rate is zero, both drive and sense systems oscillate at the same frequency. As the input rate is increased, there appear two resonances for both drive and sense modes (total of 4 resonances; drive system has two resonances, sense system has two resonances). One set of the resonances shifts down with the input rate linearly whereas the other set increases.

Figure 4.4: Resonant frequencies of 3 designs for linear 2-DOF Vibratory Gyroscopes while $\Omega_z \neq 0$ and $Q_d = Q_s = 1000$. Each curve represents two resonances; one for drive, the other for sense.
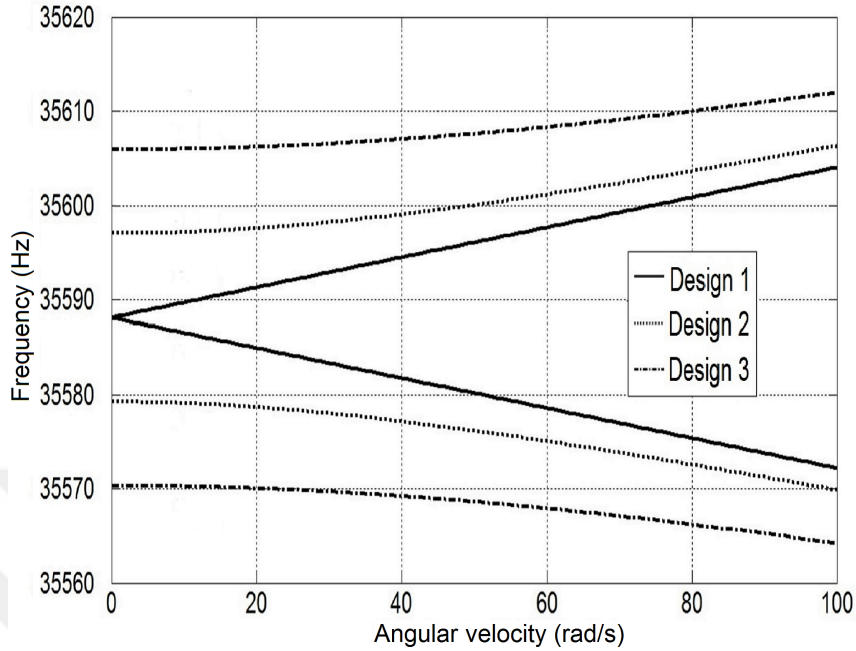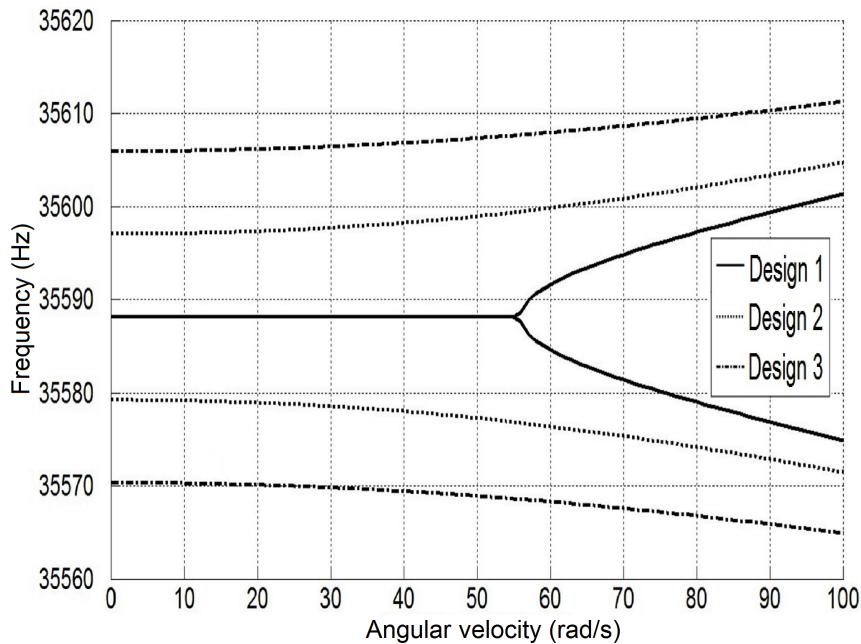

Figure 4.5: Resonant frequencies of 3 designs for linear 2-DOF Vibratory Gyroscopes while $\Omega_z \neq 0$ and $Q_s = 500$, $Q_d = 1000$. Each curve represents two resonances; one for drive, the other for sense.

For the other designs (Design 2 and 3) there is a non-linear relation between the resonance shift and the input rate as demonstrated in Fig. 4.4. In general, if sense and drive resonances are placed away from each other, the effect of the frequency shift diminishes.

In Fig. 4.5, it is illustrated the shift in the resonance when the drive and sense systems have different Q values. For perfectly match gyro (Design 1), the resonant frequencies do not shift until the rate is increased above certain value which is 56 rad/s in this example. Beyond this rate a frequency shift is again observed. Design 2 and Design 3, on the other hand behave as same as the designs shown in Fig. 2, in terms of resonant frequencies.

Next, we calculated the frequency responses of drive and sense systems. Fig. 4.6 and 4.7 show drive mode amplitude (x_0) and sense mode amplitude (y_0) respectively, calculated using equation (4.4). In Fig. 4.6, it is assumed that the drive system is driven by a constant force to get 1 μm peak vibration amplitude at the resonance when there is no input rate. As the input rate increases the amplitude drops and frequency shifting occurs in consistent with Fig. 4.4. For the calculations in Fig. 4.6, we assumed the drive system is driven by a constant force. However, in a gyro system, the drive amplitude is kept constant by a feedback loop. This will be considered later. For the sense system, when there is no input rate, there is no sense mode vibration. As the input rate increases the sense system starts vibrating due to the coupling of drive system through Coriolis and centrifugal force. As a result the amplitude increases and also frequency shifting occurs as shown in the figure.

We also plotted the curve corresponding to the 150 rad/sec input rate in Fig. 4.8 to illustrate the effect of Coriolis force and the Centrifugal force, separately. As shown in the figure, the main source of frequency shift and amplitude variation is the Coriolis force. One can neglect the centrifugal force.
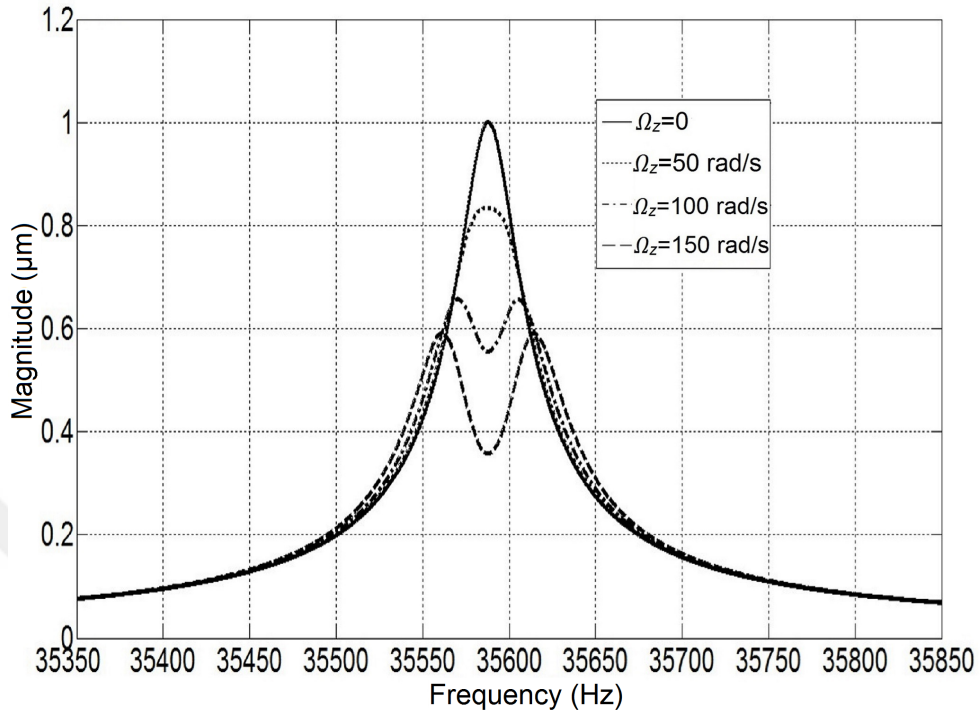
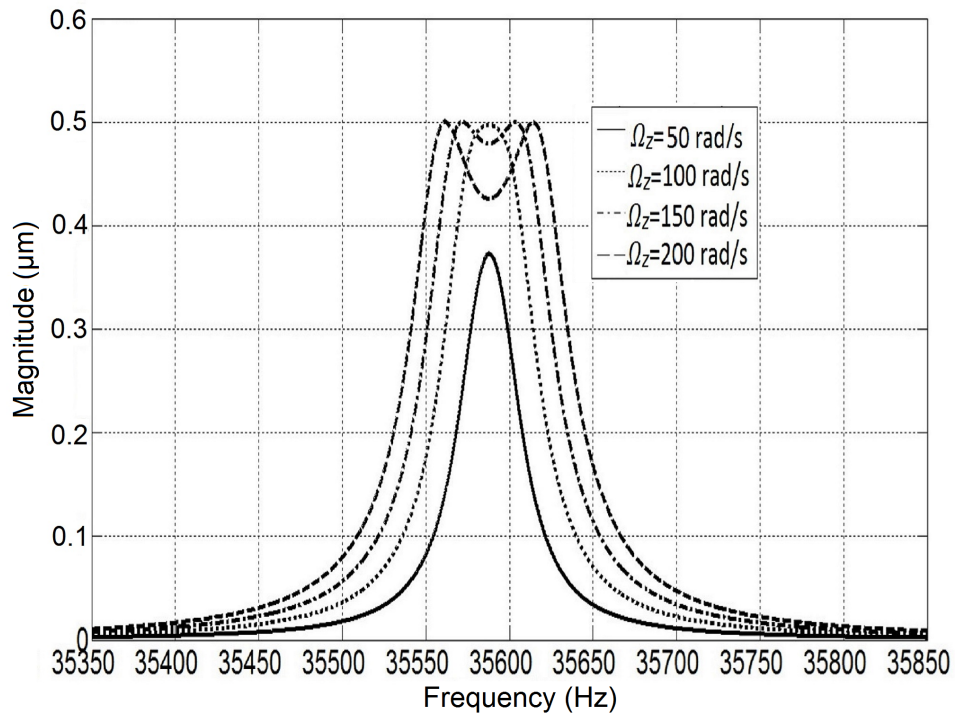Figure 4.6: Amplitude of the drive mode of Design 1 where $Q_d = Q_s = 1000$.

Figure 4.7: Amplitude of the sense mode of Design 1 where $Q_d = Q_s = 1000$.
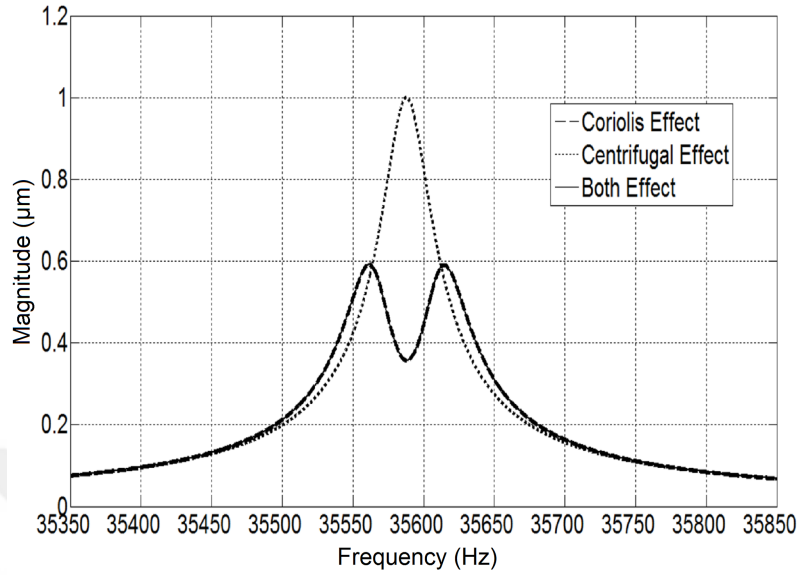
Figure 4.8: Amplitude of the drive mode of Design 1 where $Q_d = Q_s = 1000$ and $\Omega_z = 150$ rad/s with the effect of Coriolis force, the Centrifugal force and both of them.

In general, the resonant frequency shift affects the linearity of linear 2-DOF vibratory gyroscopes due to the difference between resonances of drive system proportional to angular velocity. In a typical vibratory gyroscope, the drive mode is not driven in open loop architecture but it is oscillated in a closed loop system. Therefore the drive mode tracks the Eigen frequencies of the drive system. For high input rates frequency splitting occurs. The double peaks in the spectrum will decrease the stability of the drive oscillator. Assuming the drive system is always tracking the lower frequency peak and regulating the vibration amplitude to 1 μm, one can calculate the linearity of the system. For Design 1, F_0 of the system is set such that the drive mode amplitude is 1 μm. The amplitude of the sense system is calculated at the drive frequency. The sense amplitude is a measure of the input rate. There must be a linear relation between the sense amplitude and the input rate. Fig. 4.9 plots the sense amplitude as a function of input rate for Design 1 where the modes match perfectly. As shown in Fig. 4.9, the sensitivity of the system increases as the sense Q increases, however,

60
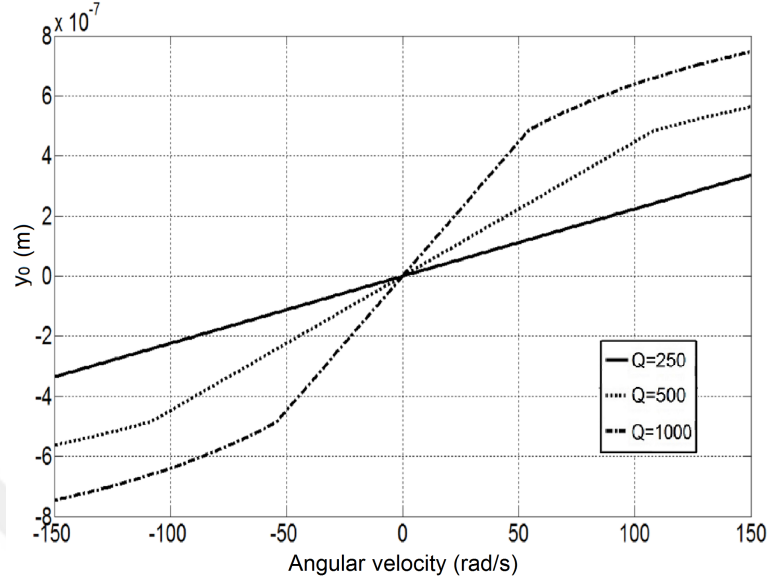
Figure 4.9: Linearity of the linear 2-DOF Vibratory Gyroscope for Design 1 where $Q = Q_d = Q_s$.
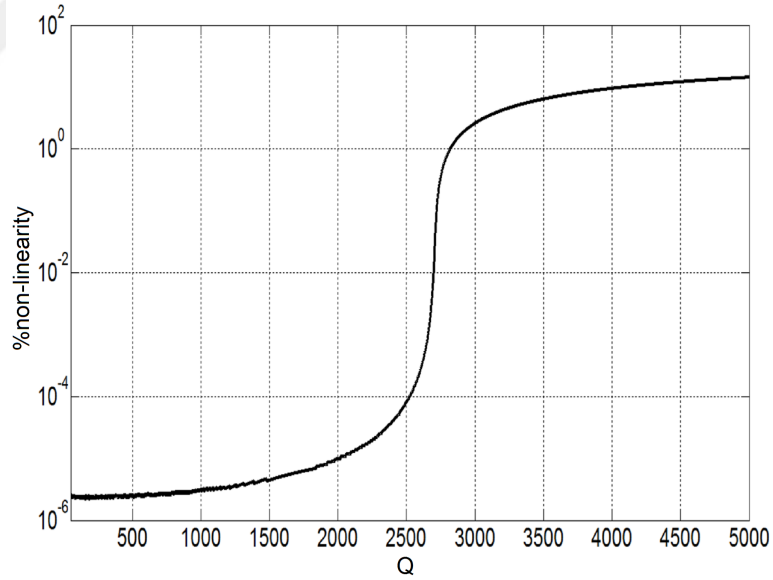
Figure 4.10: Nonlinearity of the different Q systems for Design 1 where $Q = Q_d = Q_s$.

at higher Q values the gyroscope becomes less linear. This is due to the fact that both drive and sense resonance shifts affect the amplitude of the sense system.

We also plotted the non-linearity as a function of Q. We defined the non-linearity as the maximum deviation between the gyroscope's output and the expected output as the input angular rate over the full-scale range which is as assumed to be 20 rad/s.

Fig. 4.10 plots the non-linearity as a function of Q of the gyroscope. Above Q of 3000, the non-linearity increases above 1%.

4.2.2 Torsional 2-DOF Vibratory Gyroscopes

Similarly one can also analyze the torsional micro-machined gyroscopes. These gyro systems use a rotational vibratory motion which is generated by rotational drive oscillator, vibrating at a constant angular momentum. The Coriolis torque induces a rotational motion along the sense direction which is measured by a sense-mode angular accelerometer. One of the torsional 2-DOF vibratory gyroscopes is designed as a gimbal system [42]. This gimbal system for a z-axis torsional gyroscope is shown in Fig. 4.11. The drive and sense-mode deflection angles of gyro structure are ϕ_d, ϕ_s respectively. The drive gimbal allows the proof mass to rotate along x-axis. Coriolis torque is induced along the y-axis as a response to rotation along z-axis. Assuming angular input rate is constant and the oscillation angles are small, the equation of motion is shown in (4.9) for torsional 2-DOF vibratory gyroscopes [1]. The terms of $(I_z^s + I_x^s - I_y^s)\Omega_z$ and $(I_z^s + I_y^s - I_x^s)\Omega_z$ denote Coriolis torques.
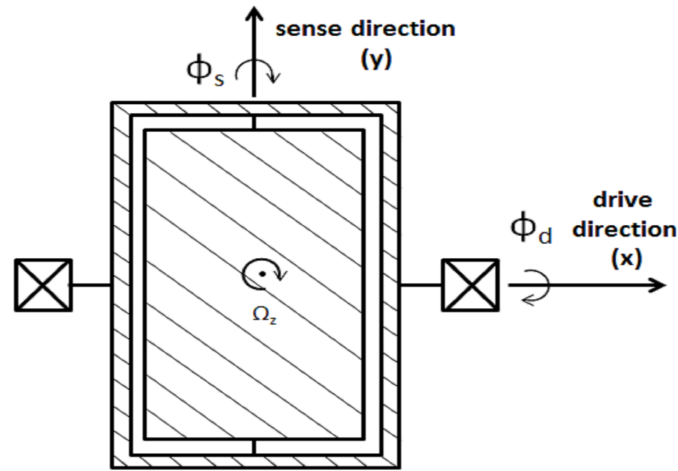

Figure 4.11: Torsional z-axis gyroscope with drive gimbal structure. Rotation axis is going through the inner mass.

$$(I_x^d + I_x^s)\ddot{\phi}_d + (C_x^d + C_x^s)\dot{\phi}_d + K_x^d\phi_d = -(I_z^s + I_x^s - I_y^s)\Omega_z\dot{\phi}_s$$

$$I_y^s\ddot{\phi}_s + C_y^s\dot{\phi}_s + K_y^s\phi_s = (I_z^s + I_y^s - I_z^s)\Omega_z\dot{\phi}_d \quad (4.9)$$

Equations of motion of the gyroscope given in (4.9) can be written in the state-space notation as:

$$X = \begin{bmatrix} \phi_d \\ \phi_s \\ \dot{\phi}_d \\ \dot{\phi}_s \end{bmatrix}, B = \begin{bmatrix} 0 \\ 0 \\ \frac{\tau_0}{(I_x^d + I_x^s)} \\ 0 \end{bmatrix} \quad (4.10)$$

$$A = \begin{bmatrix} 0 & 0 & 1 & 0 \\ 0 & 0 & 0 & 1 \\ \frac{-K_x^d}{(I_x^d + I_x^s)} & 0 & \frac{-(C_x^d + C_x^s)}{(I_x^d + I_x^s)} & \frac{-(I_z^s + I_x^s - I_y^s)\Omega_z}{(I_x^d + I_x^s)} \\ 0 & \frac{-K_y^s}{I_y^s} & \frac{(I_z^s + I_y^s - I_z^s)}{I_y^s} & \frac{-C_y^s}{I_y^s} \end{bmatrix} \quad (4.11)$$

C and D matrices are as same as in (4.7). According to (4.11) damping part of the A matrix consists of Coriolis torques and damping coefficients of the system. The spring part and moment of inertia part of the A matrix consists of only spring constants and moments of inertia of the system, respectively.

Table 4.2: 3 DESIGNS FOR TORSIONAL 2-DOF VIBRATORY GYROSCOPES AND THEIR RESONANT FREQUENCIES WHEN $\Omega_z = 0$.

Designs	K_x^d $(kg.m^2/s^2)$	K_y^s $(kg.m^2/s^2)$	f_{drive} (kHz)	f_{sense} (kHz)
Design 1	1	1	35.59	35.59
Design 2	1.0005	0.9995	35.60	35.58
Design 3	1.001	0.999	35.61	35.57

For a typical MEMS gyro, 3 designs were assumed with different spring constants around 1 $kg.m^2/s^2$ and their moment of inertias, I_x^d, I_x^s, I_y^s and I_z^s are 10×10^{-12},

10×10^{-12}, 20×10^{-12} and 200×10^{-12} kg.m^2 respectively. For these three designs, drive and sense resonant frequencies are shown in Table 4.2 for undamped case.

Figure 4.12: Resonant frequencies of 3 designs for torsional 2-DOF Vibratory Gyroscopes while $\Omega_z \neq 0$ and $Q_s = 1000$, $Q_d = 1000$. Each curve represents two resonances; one for drive, the other for sense.
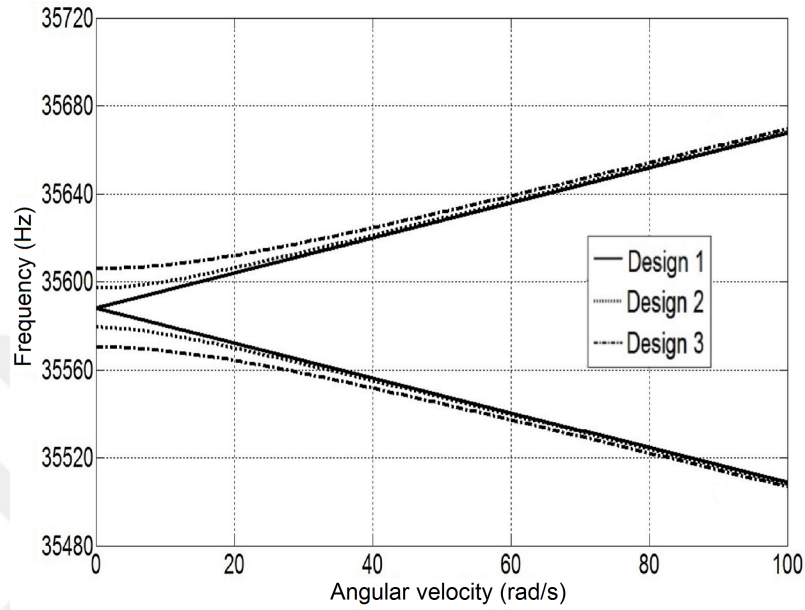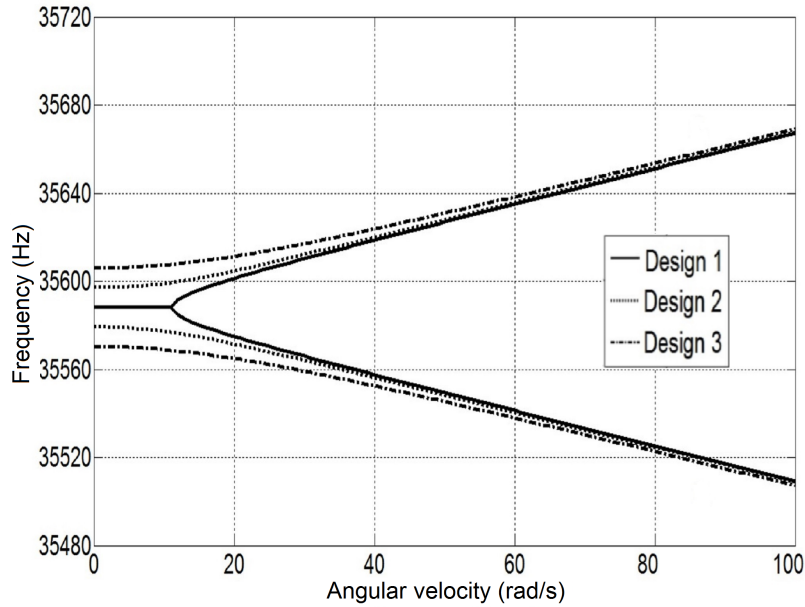

Figure 4.13: Resonant frequencies of 3 designs for torsional 2-DOF Vibratory Gyroscopes while $\Omega_z \neq 0$ and $Q_s = 500$, $Q_d = 1000$. Each curve represents two resonances; one for drive, the other for sense.
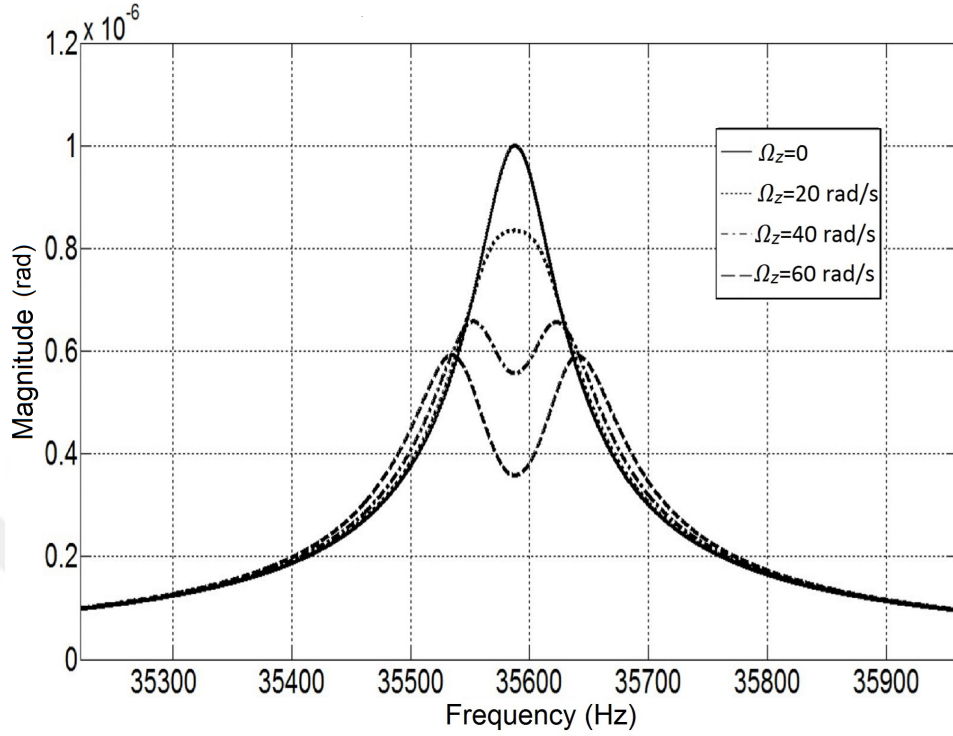
Figure 4.14: Amplitude of the drive mode of Design 1 where $Q_s = Q_d = 500$.
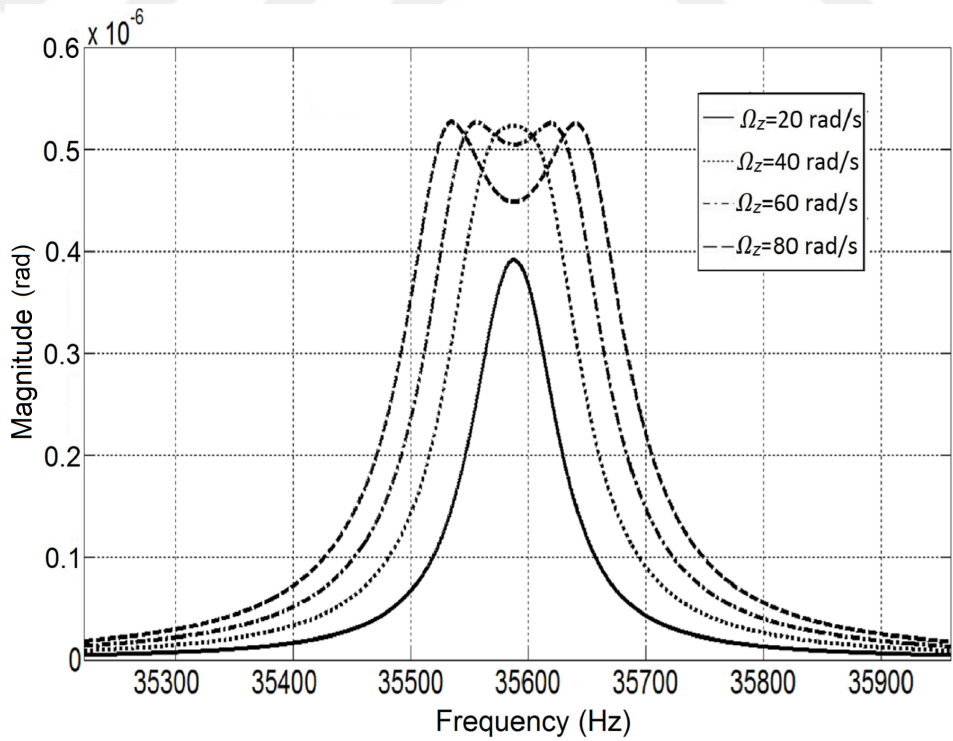
Figure 4.15: Amplitude of the sense mode of Design 1 where $Q_s = Q_d = 500$.
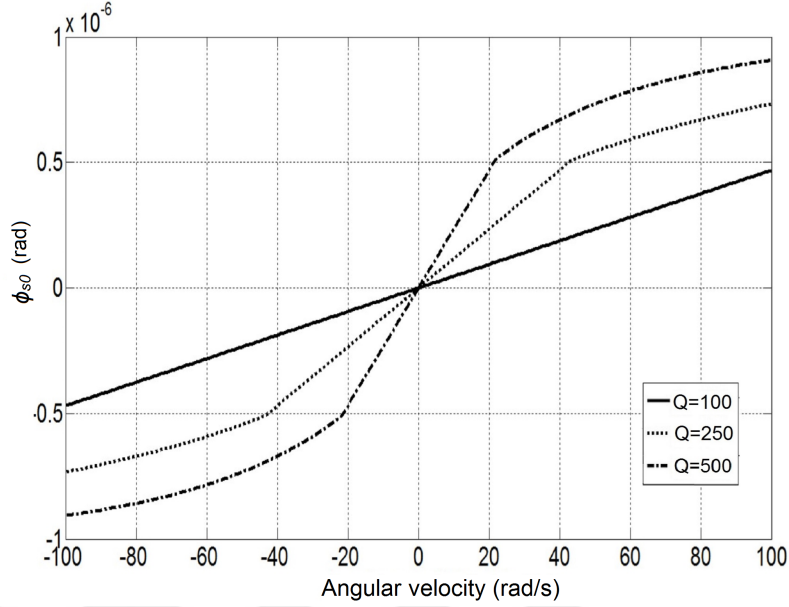
Figure 4.16: Linearity of the torsional 2-DOF Vibratory Gyroscope for Design 1 where $Q = Q_s = Q_d$.

After applying a rotation on to the system it is clearly seen that the resonant frequency of one of the modes with an applied angular velocity is linearly increasing and the other one is decreasing for mode matched design. And the effect of the frequency shift diminishes as the difference between resonant frequencies of drive and sense mode increases in Fig. 4.12.

We also investigated the effect of Q differences in the three designs. Fig. 4.13 shows the frequency shift when the drive and sense Q values are different. The biggest impact is for the mode matched case. For the mode matched case, there is no frequency shift until the input rate is increased to 11 rad/sec. As we demonstrated before for linear 2-DOF vibratory gyroscopes, the resonant frequency shift should also affect the linearity of the torsional 2-DOF vibratory gyroscopes. In torsional systems, the fundamental resonant operation principle is same as linear systems so amplitudes of drive mode ($\phi_d 0$) in Fig. 4.14 and sense mode ($\phi_s 0$) in Fig. 4.15 can be calculated from the state-space model for this structure given in (4.4).

τ_0 of the system is arranged to excite its drive mode by 10^{-6} rad for all Q values

and it is illustrated that the linearity of Design 1 is affected by different Q systems regarding to the automatic gain control feedback system in Fig. 4.16.
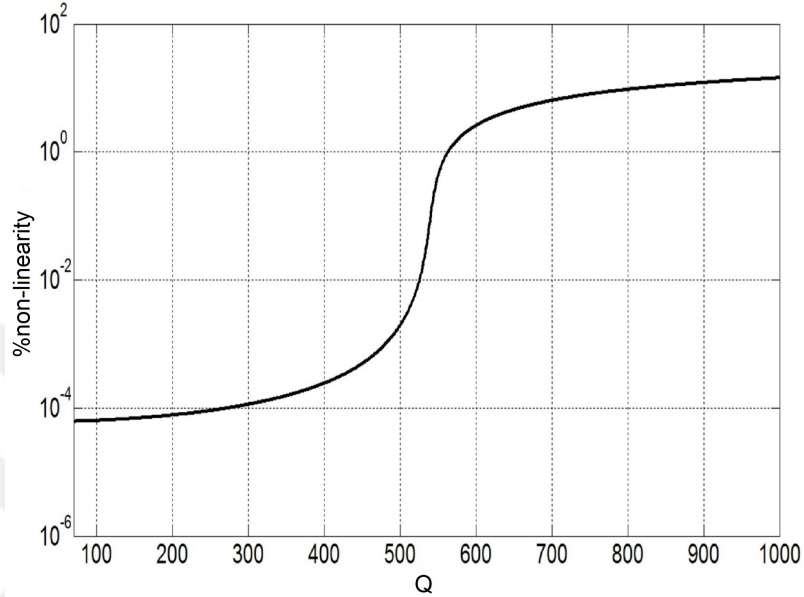
Figure 4.17: Nonlinearity of the different Q systems for Design 1 where $Q = Q_s = Q_d$.

The full-scale range is 20 rad/s and it is illustrated the change of non-linearity of Design 1 based on Q in Fig. 4.17. Above Q of 600, the non-linearity increases above 1%.

4.2.3 Multi-DOF Vibratory Gyroscopes

There are various multi-DOF vibratory gyroscopes in the literature. Examples include 3-DOF systems with 2-DOF sense-mode and 1-DOF drive mode architecture [38], 4-DOF system with 2-DOF drive and 2-DOF sense-modes [43]. In this section we examined 3-DOF vibratory gyroscope with 2-DOF sense-mode architecture as shown in Fig. 4.18. This multi-DOF gyroscope system has a 2-DOF sense-mode oscillator and a 1-DOF drive-mode oscillator. Two interconnected proof masses are attached to the decoupling frame through m_1. The proof masses, m_1 and m_2 oscillate together in the drive-direction and they form 1-DOF oscillator in the drive mode along with the spring k_{1x}. The sense system is more complex. The proof masses move in the senses
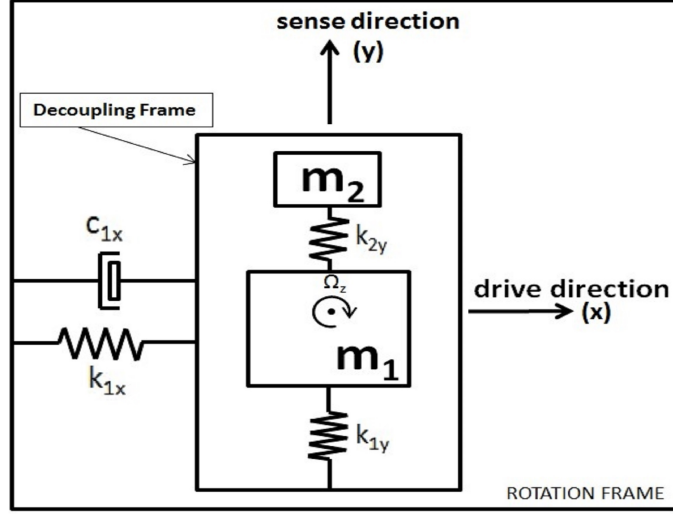
Figure 4.18: Mass-spring-damper system of the 3-DOF Vibratory Gyroscope with 2-DOF sense-mode architecture.

direction and for the 2-DOF oscillator along with k_{1y} and k_{2y}. According to [1], the equation of motion is shown in (4.12).

$$m_T\ddot{x}_1 + c_{1x}\dot{x}_1 + k_{1x}x_1 = 2m_2\Omega_z\dot{y}_2 + 2m_1\Omega_z\dot{y}_1 + m_T\Omega_z^2 x_1$$

$$m_1\ddot{y}_1 + c_{1y}\dot{y}_1 + k_{1y}y_1 = k_{2y}(y_2 - y_1) + m_1\Omega_z^2 y_1 - 2m_1\Omega_z\dot{x}_1 \qquad (4.12)$$

$$m_2\ddot{y}_2 + c_{2y}\dot{y}_2 + k_{2y}y_2 = k_{2y}y_1 + m_2\Omega_z^2 y_2 - 2m_2\Omega_z\dot{x}_1$$

Equations of motion of the gyroscope given in (4.12) can be written in the form of state-space model given in (4.4):

$$X = \begin{bmatrix} x_1 \\ y_1 \\ y_2 \\ \dot{x}_1 \\ \dot{y}_1 \\ \dot{y}_2 \end{bmatrix}, B = \begin{bmatrix} 0 \\ 0 \\ 0 \\ \frac{F_0}{m_T} \\ 0 \\ 0 \end{bmatrix}, C = \begin{bmatrix} 1 & 0 & 0 & 0 & 0 & 0 \\ 0 & 1 & 0 & 0 & 0 & 0 \end{bmatrix} \qquad (4.13)$$

$$A = \begin{bmatrix} 0 & 0 & 0 & 1 & 0 & 0 \\ 0 & 0 & 0 & 0 & 1 & 0 \\ 0 & 0 & 0 & 0 & 0 & 1 \\ -\frac{k_{1x}}{m_T} + \Omega_z^2 & 0 & 0 & -\frac{c_{1x}}{m_T} & 2\frac{m_1}{m_T}\Omega_z & 2\frac{m_2}{m_T}\Omega_z \\ 0 & -\frac{k_{1y}+k_{2y}}{m_1} + \Omega_z^2 & \frac{k_{2y}}{m_1} & -2\Omega_z & -\frac{c_{1y}}{m_1} & 0 \\ 0 & \frac{k_{2y}}{m_2} & -\frac{k_{2y}}{m_2} + \Omega_z^2 & -2\Omega_z & 0 & -\frac{c_{2y}}{m_2} \end{bmatrix} \qquad (4.14)$$

According to (4.14), damping part of the A matrix consists of Coriolis accelerations and the damping coefficients of the system. The spring part of the A matrix consists of centripetal acceleration and the spring constants of the system. Mass part of the A matrix consists of proof masses m_T, m_1 and m_2 where m_T is the total mass of the two proof masses.
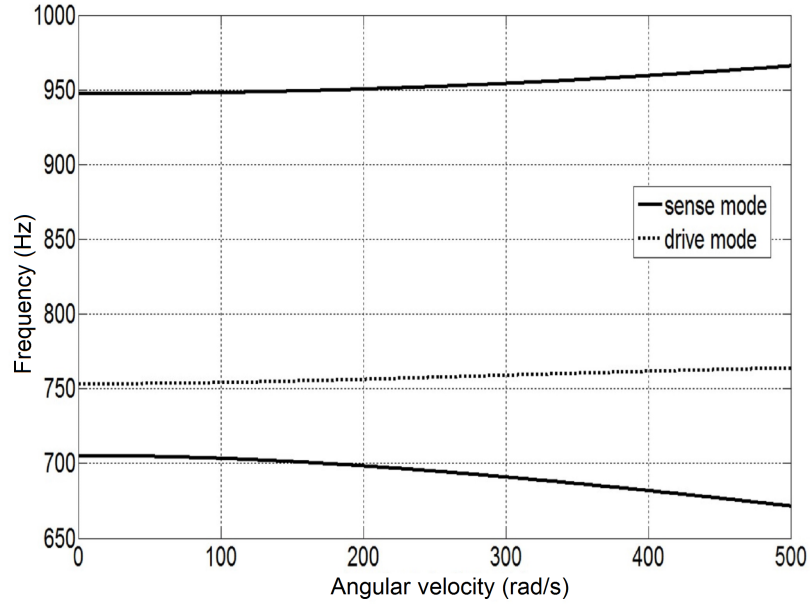
Figure 4.19: Resonances of sense and drive modes of the multi-DOF Vibratory Gyroscope while $\Omega_z \neq 0$ and $Q_s = Q_d = 1000$. Each curve represents three resonances; one for drive, the others for sense.

We used same example in [1] and for this bulk micro-machined prototype, spring constants, k_{1x}, k_{1y} and k_{2y} are 61.2, 78.4 and 3.36 N/m respectively. The proof

masses, m_1, m_1 and m_f are 2.46x10^{-6} kg, 1.54x10^{-7} and 1.19x10^{-7}. Their drive and sense resonant frequencies are calculated by the Eigen values of A matrix given in (4.14) and showed for undamped case in Fig. 4.18. There are 6 Eigen values as two complex conjugates where the imaginary part shows the resonant frequency. We used these values to calculate the resonant frequencies for this example design in Fig. 4.19.
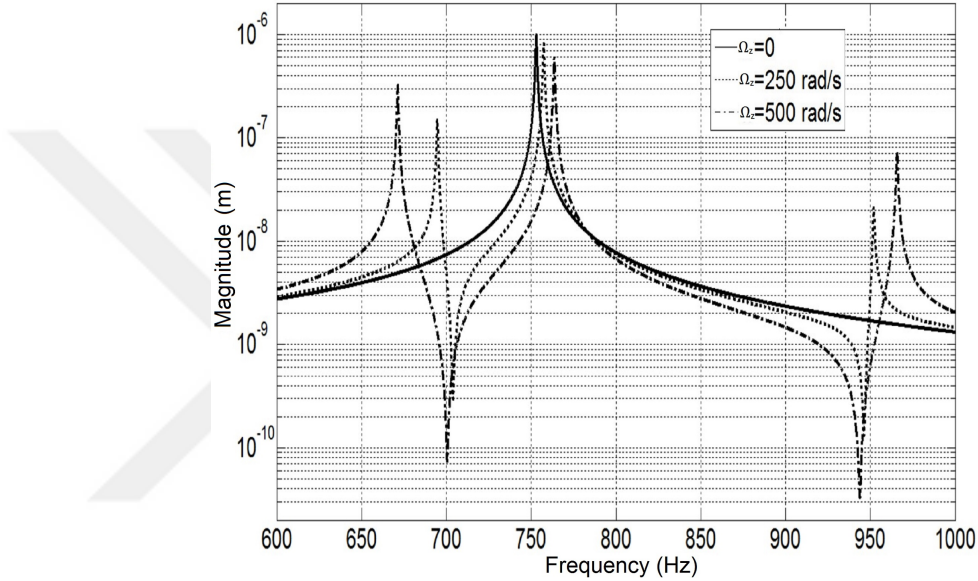
Figure 4.20: Amplitude of the drive mode where $Q_s = Q_d = 1000$.
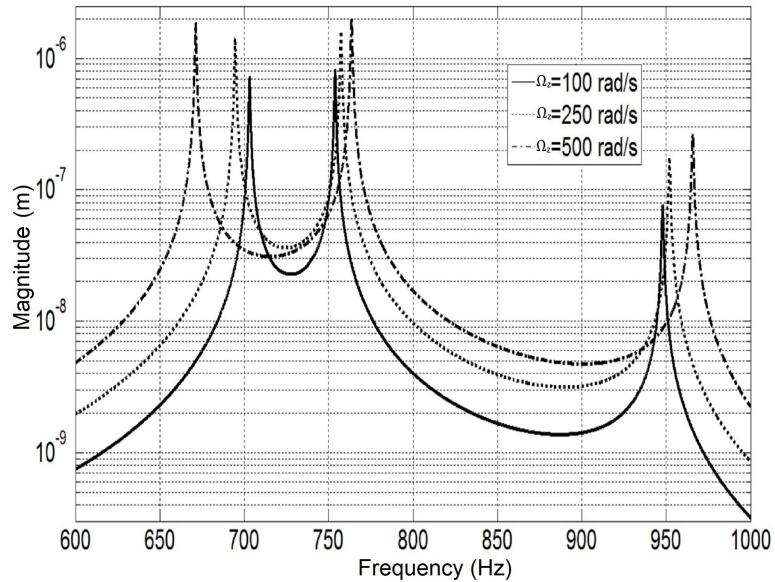
Figure 4.21: Amplitude of the sense mode where $Q_s = Q_d = 1000$.

With the applied input rate, the resonant frequencies shift. In this example, we did not observe frequency splitting for the drive mode, and the drive mode resonance increases as shown in Fig. 4.19. The two sense modes on the other hand move away from each other with the increased input rate.

This frequency shift affects the linearity of the multi-DOF vibratory gyroscopes as in the case of linear 2-DOF vibratory gyroscopes. Amplitudes of drive mode (x_0) in Fig. 4.20 and sense mode (y_{02}) in Fig. 4.21 can be calculated from the state-space model given in (4.4).
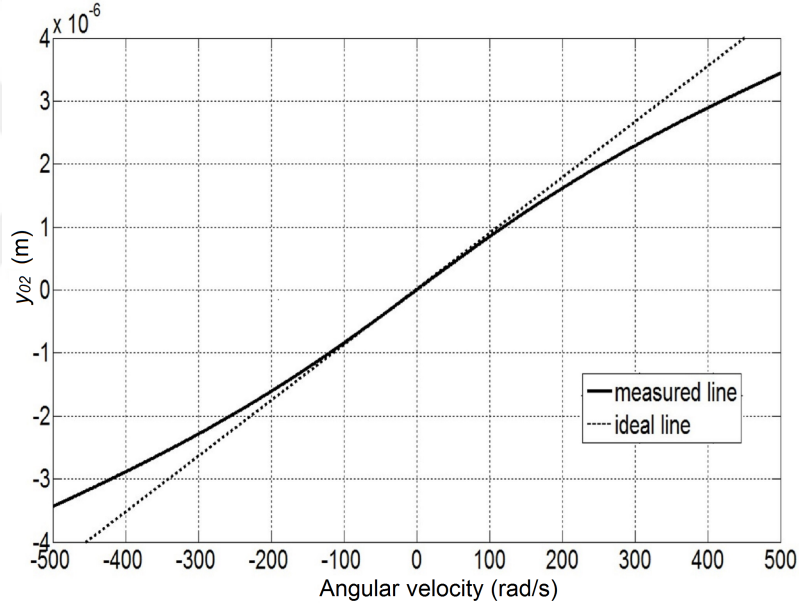
Figure 4.22: Linearity of the 3-DOF Vibratory Gyroscope where $Q_s = Q_d = 1000$.

To assess the linearity of the gyro system, we assumed that F_0 of the system is adjusted to excite the drive mode by 1 μm with an automatic gain control feedback system. Then we calculated the sense response as shown in Fig. 4.22. The non-linearity is calculated as 0.0145 % for the full-scale range is 20 rad/s. In this case, the non-linearity is very small compared to that of 2-DOF gyro systems, and based on our calculations, the Q of the drive and sense resonances have minimal effect of the non-linearity.

4.2.4 Ring Vibratory Gyroscopes

One of the examples of microfabricated gyroscopes is the vibrating ring gyroscope which consists of an elastic ring symmetrically supported by the eight identical semi-circular springs [35] as shown in Fig. 4.23. The gyroscope was fabricated using HARPSS fabrication process [44]. This process allows fabrication of high aspect ratio structures made of poly-silicon. (Youngs modulus, E = 150 GPa, density, $\rho = 2.328$ g/cm). The outer ring diameter is 1.1 mm and the ring width is 4 μm. The thickness of the structure is 80 μm. The support diameter is 120 μm and it is anchored to the substrate. The supporting springs are in the shape of arcs which diameter is 470 μm. In this design, the ring is excited at the primary flexural mode at a fixed amplitude electrostatically and the secondary flexural mode is formed at 45°. Coriolis force causes the energy transfer from the primary mode to the secondary flexural mode when the rotation is applied and this amplifies the latter mode which can be detected capacitively.

Figure 4.23: The HARPSS Vibrating Ring Gyroscope.

Mode 1

(a)

Mode 2
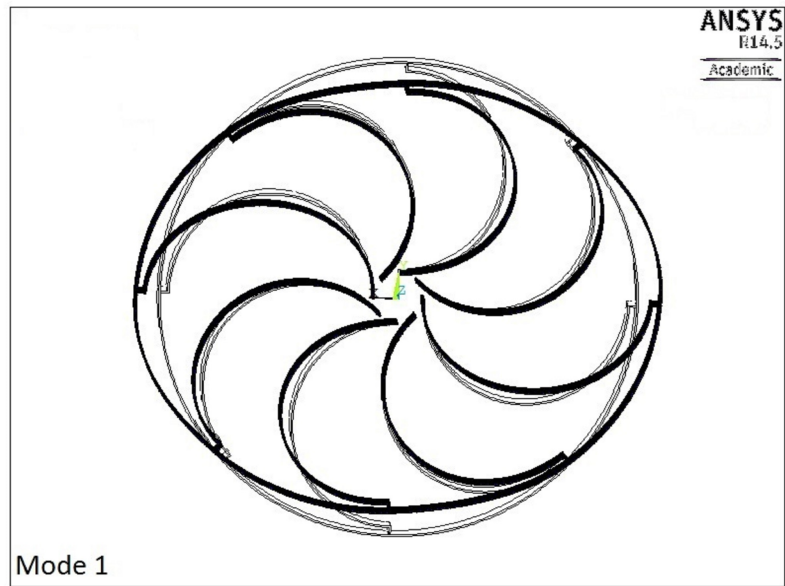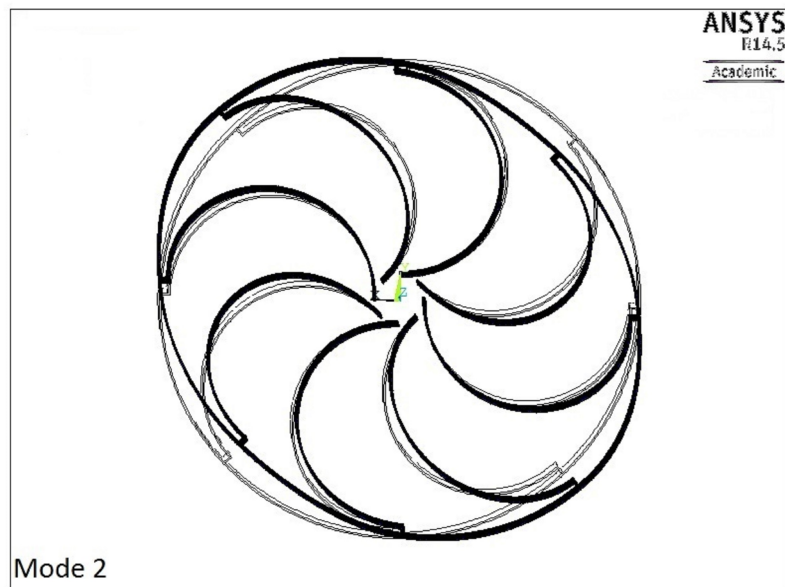
(b)

Figure 4.24: Finite Element Analysis of the HARPSS Ring Gyroscope (a) Primary flexural mode (b) Secondary flexural mode.

For the structure described above, we performed modal analysis using ANSYS Simulation Tool. BEAM 188 elements were used and rotating reference frame was defined with Coriolis option on. The geometry was clamped to support the post at the center. The first vibrational mode is torsional at about 10 kHz; next two modes are translational at about 20 kHz. The fourth and fifth modes are the ones that are used in the gyroscope. These were flexure modes at 28.42 kHz. Mode shapes for the first two flexural modes of this geometry are shown in Fig. 4.24. The mode shape of the second mode is 45° degree rotated version of the first mode.

This ring architecture is similar to 2-DOF linear system. However, sense mode of the ring gyroscope is 45° rotated instead of 90° from its drive mode compared to other linear gyros. Therefore one can use 2-DOF gyro equations for ring gyroscopes. The A matrix is given by,

$$A = \begin{bmatrix} 0 & 0 & 1 & 0 \\ 0 & 0 & 0 & 1 \\ \frac{-k_x}{m} + \Omega_z^2 & 0 & \frac{-c_x}{m} & -2\Omega_z \sin 45° \\ 0 & \frac{-k_y}{m} + \Omega_z^2 & 2\Omega_z \sin 45° & \frac{-c_y}{m} \end{bmatrix} \tag{4.15}$$

To obtain spring constant, mass and the damping coefficient we used harmonic analysis tool of ANSYS. First, we excited the primary flexural mode of the vibrating ring gyroscope by applying outward forces at its top and bottom nodes. The spring constant $(k = k_x = k_y)$ of the system can be calculated from the amplitude of the drive mode (x) at low frequencies and the applied force (F). The modal mass (m) at 28.42 kHz can be calculated by using the spring constant $(\omega_0 = \sqrt{k/m})$. Damping coefficient $(c = c_x = c_y)$ is applied by the user. We compared the Eigen value calculations of A matrix against ANSYS modal analysis results. We got a very good match between ANSYS and Eigen value calculations as shown in Fig. 4.25. The frequency of the first flexural modes is 28.42 kHz. As the input rate increases, there
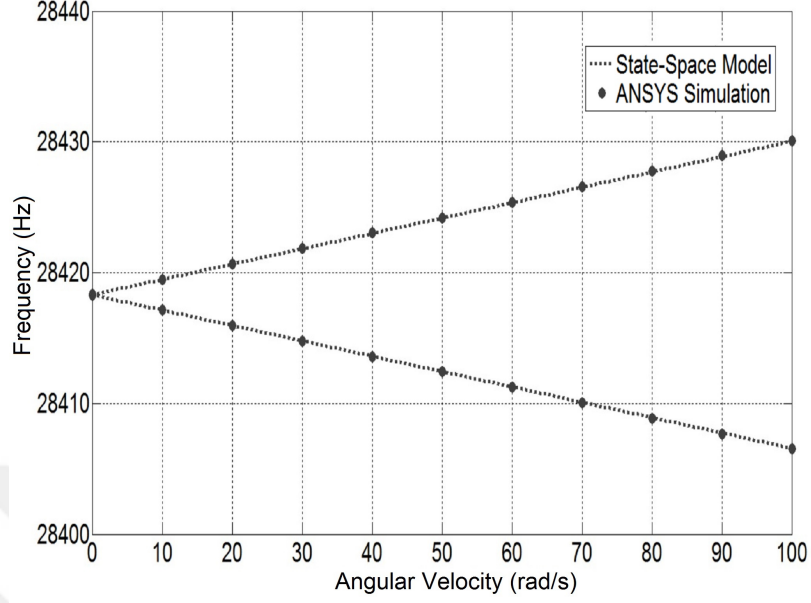
Figure 4.25: ANSYS and state-space model results for the resonances of sense and drive modes of the HARPSS Vibrating Ring Gyroscope while $\Omega_z \neq 0$ and $Q_s = Q_d = 5000$. Each curve represents two resonances; one for drive, the other for sense.

appear two resonances. One of the resonant frequency increases linearly, whereas the second resonant frequency decreases as the input rate increases.

In this system, the fundamental resonant operation principle is same as linear systems so the amplitude of drive mode can be calculated by harmonic analysis with ANSYS Simulation Tool. We excited the primary flexural mode of the vibrating ring gyroscope by applying outward forces, 10^{-8} N at its top and bottom nodes to get 1 μm radial motion and the damping ratio is 10^{-4}. The spring constant $(k = k_x = k_y)$ of the system can be calculated by the amplitude of drive mode (x) at low frequencies and applied force (F). The modal mass (m) can be also calculated at 28.42 kHz by the calculated spring constant (k). So one can also acquire the damping coefficient $(c = c_x = c_y)$ of this system.

Fig. 4.26 and 4.27 show drive mode amplitude (x_0) and sense mode amplitude (y_0) respectively, calculated using equation (4.4). In Fig. 4.26, it is assumed that the drive system is driven by a constant force to get 1 μm peak vibration amplitude at

75
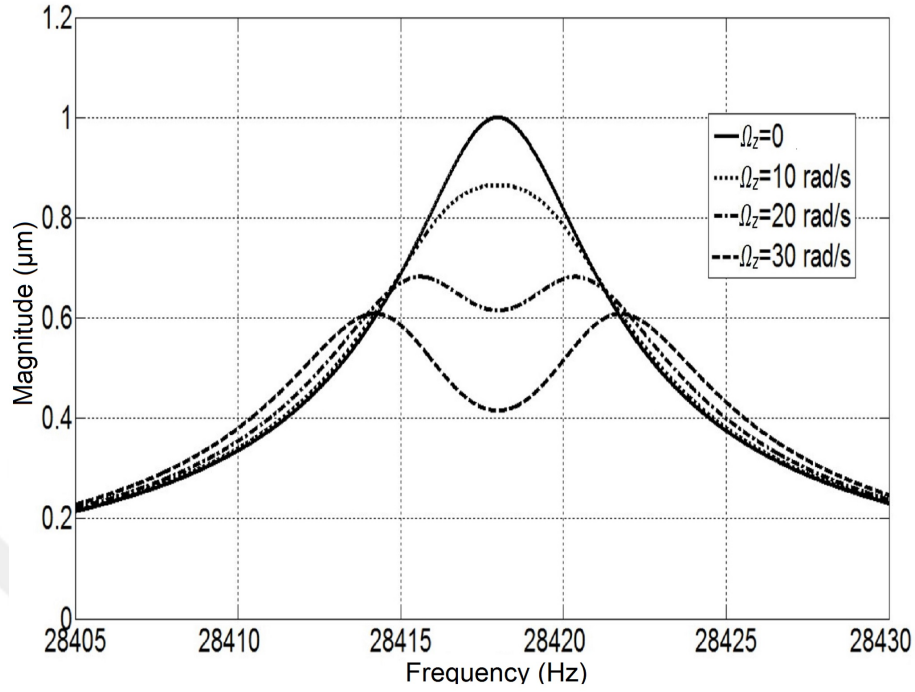
Figure 4.26: Amplitude of the drive mode for the HARPSS Vibrating Ring Gyroscope where $Q_s = Q_d = 5000$ (Damping coefficient is 10^{-4} N.s/m).
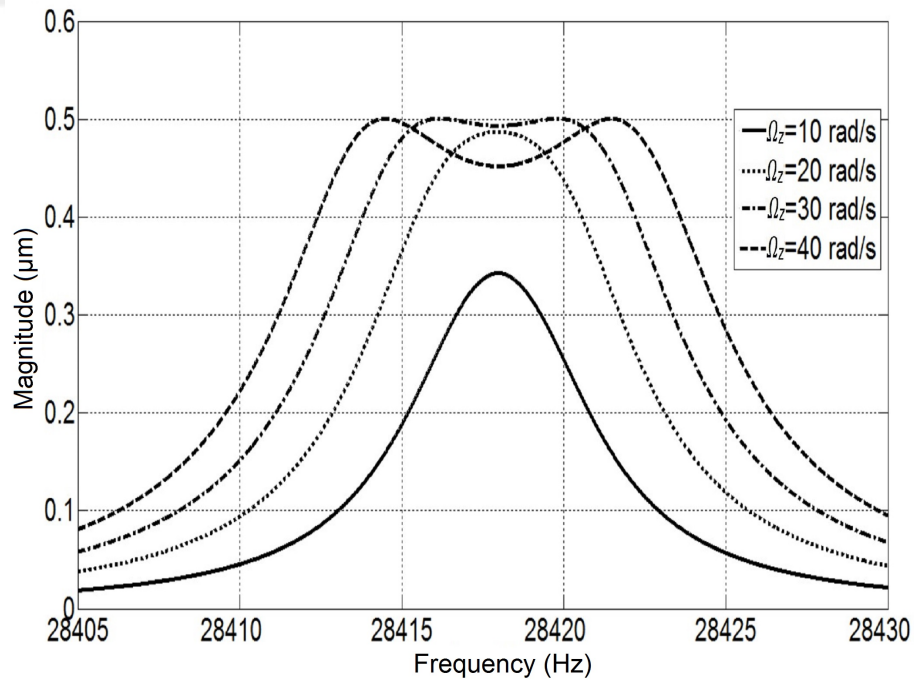
Figure 4.27: Amplitude of the sense mode for the HARPSS Vibrating Ring Gyroscope where $Q_s = Q_d = 5000$ (Damping coefficient is 10^{-4} N.s/m).
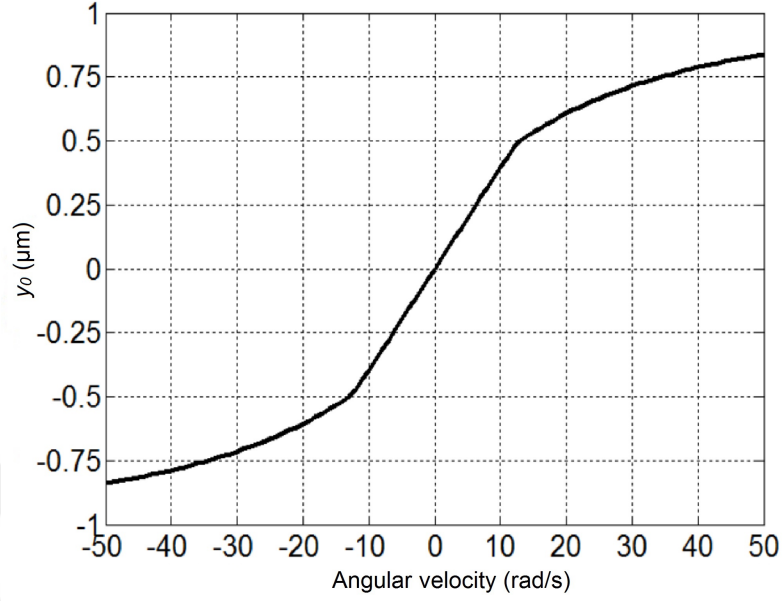
Figure 4.28: Linearity of the HARPSS Vibrating Ring Gyroscope where $Q_s = Q_d = 5000$.

the resonance when there is no input rate. As the input rate increases the amplitude drops and frequency shifting occurs in consistent with Fig. 4.25. For the sense system, when there is no input rate, there is no sense mode vibration. As the input rate increases the sense system starts vibrating due to the coupling of drive system through Coriolis and centrifugal force. As a result the amplitude increases and also frequency shifting occurs as shown in the figure.

F_0 of the system is arranged to excite its drive mode by 1 μm with an automatic gain control feedback system and it is illustrated that the linearity of this gyro structure is shown in Fig. 4.28. According to Fig. 4.28 non-linearity is calculated as 15.3% since the full-scale range is taken as 20 rad/s.

4.3   Discussion

In this chapter, we presented a thorough analysis of gyroscope systems including the coupling between the drive and sense systems due to Coriolis force and centrifugal force. Our analysis showed that the main coupling mechanism between the drive

and sense modes is through the Coriolis force and the effect of centrifugal force can be neglected. The Coriolis force changes the damping of the system affecting the resonant frequencies. The analysis was applied to both mode matched and multi-DOF gyroscope systems. The most important finding of the analysis is the fact that the resonance frequencies of the drive and sense modes shift with the input rotation. This affects the linearity of the gyroscope systems by setting a fundamental limit for the linearity. For gyroscopes with high input range lowering the Q may result in more linear response sacrificing the sensitivity for mode matched gyroscopes. For non-mode matched gyroscopes the non-linearity due to frequency shifting is minimal. On the other hand, all gyroscopes should be prone to quality factor widening at high input rates. The frequency splitting observed in the drive mode may result in reduced stability of the drive mode oscillators. Double peaking may result in sudden frequency jumps at large input rates for the drive loop oscillator increasing the output noise. We do not have an immediate solution for this problem. Lowering Q may solve the problem but the overall stability of the oscillator will be sacrificed in this case. More detailed analysis has to be performed to address this issue.

CHAPTER V

CONCLUSION AND FUTURE WORK

In this work, we introduced waveguide based gyroscopes and performed in depth analysis of vibrating gyroscope systems. The novel gyroscope uses the acoustic modes of a ring shaped waveguide. The rotation measurement method is based on the phase shift of traveling waves. In this thesis, we showed how to calculate the modes of a waveguide and chose the most appropriate mode for the detection. The flexural modes are especially suitable for this kind of gyroscopes due to their direction of particle motion. One can excite two of these modes propagating in the opposite directions through the closed loop waveguide. The excitation transducers can also collect the waves, after they complete propagation through the ring. Ideally, when there is no rotation, there exists no phase shift between the two waves. If a rotation is introduced, the phase shift reveal proportional to the amount of rotation. Alternatively, the resonances of the ring can be observed. Due to the phase shift of the propagating waves, the resonance frequencies shift. By observing the frequency shift one can measure the rotation rate.

The observation of frequency shift in the resonances of a ring motivated us to observe the resonances of vibratory gyroscopes. We performed in depth analysis of vibratory gyroscopes. Until now, the vibratory gyroscopes were analyzed by separating the drive and sense systems. First we coupled the two systems through Coriolis force. We built a systematic approach by using the state space representation to find resonances as well as vibration amplitudes. Our analysis revealed that drive and sense resonances shift with the application of rotation. The shift is due to the Coriolis force and Centrifugal force has minimal effect on the shift. Based on this observation, we

concluded that one can ignore the centrifugal force coupling between the drive and sense systems but can not ignore the coupling due to Coriolis force. Further analysis revealed that the resonance shift affects the linearity of vibratory gyroscopes. Especially for mode matched gyroscopes there is a fundamental limit for the linearity. Moreover, we also observed resonance broadening and splitting resonances in the frequency spectrum of both drive and sense systems. The frequency broadening in the drive system reduces the stability of the drive oscillator.

In the future, we would like to build the waveguide based gyroscope experimentally and demonstrate the operation of this device. Further detailed analysis is required to calculate the sensitivity of these devices. Also, we would like to extend the analysis of resonance shift and calculate the stability of drive system in an oscillation loop. Regarding to the resonance shift, we would like to calculate the Allan variance of a gyroscope and to understand the fundamental limits of these devices.

Bibliography

[1] C. Acar and A. Shkel, *MEMS vibratory gyroscopes: structural approaches to improve robustness.* Springer Science & Business Media, 2008.

[2] K. Funk, H. Emmerich, A. Schilp, M. Offenberg, R. Neul, and F. Larmer, "A surface micromachined silicon gyroscope using a thick polysilicon layer," in *Micro Electro Mechanical Systems, 1999. MEMS'99. Twelfth IEEE International Conference on*, pp. 57–60, IEEE, 1999.

[3] S. Datta, *Surface acoustic wave devices.* Prentice Hall, 1986.

[4] Q. Yan, Y. Wei, M. Shen, J. Zhu, and Y. Li, "Theoretical and experimental study of surface acoustic wave gyroscopic effect," in *2007 International Conference on Mechatronics and Automation*, pp. 3812–3816, IEEE, 2007.

[5] V. Varadan, W. Suh, P. Xavier, K. Jose, and V. Varadan, "Design and development of a MEMS-IDT gyroscope," *Smart Materials and Structures*, vol. 9, no. 6, p. 898, 2000.

[6] E. J. Post, "Sagnac effect," *Reviews of Modern Physics*, vol. 39, no. 2, p. 475, 1967.

[7] A. Kersey, A. Dandridge, and W. Burns, "Fiber optic gyroscope technology," *Optics News*, vol. 15, no. 11, pp. 12–19, 1989.

[8] B. A. Auld, *Acoustic fields and waves in solids*, vol. 2. RE Krieger, 1990.

[9] M. Kurosawa, Y. Fukuda, M. Takasaki, and T. Higuchi, "A surface acoustic wave gyro sensor," in *Solid State Sensors and Actuators, 1997. TRANSDUCERS'97 Chicago., 1997 International Conference on*, vol. 2, pp. 863–866, IEEE, 1997.

[10] K. Jose, W. Suh, P. Xavier, V. Varadan, and V. Varadan, "Surface acoustic wave MEMS gyroscope," *Wave motion*, vol. 36, no. 4, pp. 367–381, 2002.

[11] A. Mehta, K. Jose, and V. K. Varadan, "Numerical simulation of a surface acoustic wave (SAW) gyroscope using HP Eesof," in *SPIE's 9th Annual International Symposium on Smart Structures and Materials*, pp. 169–177, International Society for Optics and Photonics, 2002.

[12] H. Oh, S. Yang, and K. Lee, "Development of surface acoustic wave-based microgyroscope utilizing progressive wave," *Japanese Journal of Applied Physics*, vol. 49, no. 6S, p. 06GN16, 2010.

[13] W. Wang, J. Liu, X. Xie, M. Liu, and S. He, "Development of a new surface acoustic wave based gyroscope on a X-112 Y LiTaO3 substrate," *Sensors*, vol. 11, no. 11, pp. 10894–10906, 2011.

[14] H. Oh, S. S. Yang, and K. Lee, "Development of passive surface acoustic wave gyroscope with standing wave mode," in *Micro Electro Mechanical Systems (MEMS), 2011 IEEE 24th International Conference on*, pp. 565–568, IEEE, 2011.

[15] H. Tiersten, D. Stevens, and P. Das, "Circulating flexural wave rotation rate sensor," in *1981 Ultrasonics Symposium*, pp. 163–166, IEEE, 1981.

[16] B. Y. Lao, "Gyroscopic effect in surface acoustic waves," in *1980 Ultrasonics Symposium*, pp. 687–691, IEEE, 1980.

[17] G. Sagnac, "L'éther lumineux démontré par l'effet du vent relatif d'éther dans un interféromètre en rotation uniforme," *CR Acad. Sci.*, vol. 157, pp. 708–710, 1913.

[18] W. M. Macek and D. Davis Jr, "Rotation rate sensing with traveling-wave ring lasers," *Applied Physics Letters*, vol. 2, no. 3, pp. 67–68, 1963.

[19] V. Vali and R. Shorthill, "Fiber ring interferometer," *Appl. Opt*, vol. 15, no. 5, pp. 1099–1100, 1976.

[20] S. Ezekiel and G. Knausenberger, "Laser inertial rotation sensors; proceedings of the seminar, san diego, calif., august 30, 31, 1978," in *Laser inertial rotation sensors*, vol. 157, 1978.

[21] W. Chow, J. Gea-Banacloche, L. Pedrotti, V. Sanders, W. Schleich, and M. Scully, "The ring laser gyro," *Reviews of Modern Physics*, vol. 57, no. 1, p. 61, 1985.

[22] S. Ezekiel and S. Balsamo, "Passive ring resonator laser gyroscope," *Applied Physics Letters*, vol. 30, no. 9, pp. 478–480, 1977.

[23] M. Faucheux, D. Fayoux, and J. Roland, "The ring laser gyro," *Journal of optics*, vol. 19, no. 3, p. 101, 1988.

[24] M. Kayton and W. R. Fried, *Avionics navigation systems*. John Wiley & Sons, 1997.

[25] D. A. Tazartes, J. G. Mark, and R. E. Ebner, "Ring laser gyroscope dither drive system and method," Jan. 1 1991. US Patent 4,981,359.

[26] G. Pircher and G. Hepner, "Perfectionnements aux dispositifs du type du type gyrometre interferometrique a laser," 1967. French patent 1,563,720.

[27] H. C. Lefevre, *The fiber-optic gyroscope*. Artech house, 2014.

[28] S. Donati and V. A. Lodi, "Fiber gyroscope with dual frequency laser," in *Proc. ICALEO*, pp. 85–9, 1982.

[29] R. Bergh, H. Lefevre, and H. Shaw, "All-single-mode fiber-optic gyroscope with long-term stability," *Optics Letters*, vol. 6, no. 10, pp. 502–504, 1981.

[30] R. H. Dixon and J. Bouchaud, "Markets and applications for MEMS inertial sensors," in *MOEMS-MEMS 2006 Micro and Nanofabrication*, pp. 611306–611306, International Society for Optics and Photonics, 2006.

[31] M. Tanaka, "An industrial and applied review of new MEMS devices features," *Microelectronic engineering*, vol. 84, no. 5, pp. 1341–1344, 2007.

[32] D. K. Shaeffer, "MEMS inertial sensors: A tutorial overview," *IEEE Communications Magazine*, vol. 51, no. 4, pp. 100–109, 2013.

[33] N. Yazdi, F. Ayazi, and K. Najafi, "Micromachined inertial sensors," *Proceedings of the IEEE*, vol. 86, no. 8, pp. 1640–1659, 1998.

[34] J. Raper, G. Gartner, H. Karimi, and C. Rizos, "A critical evaluation of location based services and their potential," *Journal of Location Based Services*, vol. 1, no. 1, pp. 5–45, 2007.

[35] F. Ayazi and K. Najafi, "A HARPSS polysilicon vibrating ring gyroscope," *Journal of microelectromechanical systems*, vol. 10, no. 2, pp. 169–179, 2001.

[36] A. M. Shkel *et al.*, "Type I and type II micromachined vibratory gyroscopes," in *Position, Location, and Navigation Symposium, San Diego*, pp. 25–27, 2006.

[37] T. M. Mochida, Y. and K. Ohwada, "A micromachined vibrating rate gyroscope with independent beams for the drive and detection modes," *Sensors and Actuators A: Physical*, vol. 80, no. 2, pp. 170–178, 2000.

[38] C. Acar and A. M. Shkel, "Inherently robust micromachined gyroscopes with 2-DOF sense-mode oscillator," *Journal of Microelectromechanical Systems*, vol. 15, no. 2, pp. 380–387, 2006.

[39] M. I. Friswell, *Dynamics of rotating machines.* Cambridge University Press, 2010.

[40] R. Eley, C. Fox, and S. McWilliam, "Coriolis coupling effects on the vibration of rotating rings," *Journal of sound and vibration*, vol. 238, no. 3, pp. 459–480, 2000.

[41] H. Moussa and R. Bourquin, "Theory of direct frequency output vibrating gyroscopes," *IEEE Sensors Journal*, vol. 6, no. 2, pp. 310–315, 2006.

[42] H. Kuisma, T. Ryhanen, J. Lahdenpera, E. Punkka, S. Ruotsalainen, T. Sillanpaa, and H. Seppa, "A bulk micromachined silicon angular rate sensor," in *Solid State Sensors and Actuators, 1997. TRANSDUCERS'97 Chicago., 1997 International Conference on*, vol. 2, pp. 875–878, IEEE, 1997.

[43] C. Acar and A. Shkel, "Four degrees-of-freedom micromachined gyroscope," Master's thesis, University of California, Irvine, 2001.

[44] F. Ayazi and K. Najafi, "High aspect-ratio combined poly and single-crystal silicon (HARPSS) MEMS technology," *Journal of Microelectromechanical Systems*, vol. 9, no. 3, pp. 288–294, 2000.